

Edge Wetting: Steady State of Rivulets in Wedges

Nikolai Kubochkin*
Tatiana Gambaryan-Roisman†

Institute for Technical Thermodynamics, Technische Universität Darmstadt
Alarich-Weiss-Straße 10, 64287, Darmstadt, Germany

Abstract

The geometry of rough, textured, fractured and porous media is topologically complicated. Those media are commonly represented by bundles of capillary tubes when modeled. However, angle-containing geometries can serve as a more realistic portrayal of their inner structure. A basic element abidingly inherent to all of them is an open wedge-like channel. The classical theory of capillarity ignoring intermolecular interactions implies that liquid entering the wedge must propagate indefinitely along its spine when the liquid-gas interface is concave. The latter is well-known as a Concus-Finn condition. In the present paper, we show that steady-state rivulets violating Concus-Finn condition can be formed in such channels when the surface forces are taken into account. We present a simple model based on the disjoining pressure approach and analyze the shape of the rivulets in the wedges. Besides, we consider a case when the walls of the wedge are soft and can be deformed by the liquid.

Keywords: edge wetting, nanochannels, wedge, disjoining pressure, Concus-Finn condition

1 Introduction

Most of surfaces, both natural and man-made, are rough or/and contain pores or cracks [1]. Usually, they are exposed to a vapor or brought in a contact with a liquid [2]. Thus, investigation of the capillary transport in rough, porous or cracked media is beneficial for various technologies, including, by not limited to, ink-jet printing and ink production [3], biophysics [4], and micro- and nanofluidics [5, 6]. Combating the climate change stimulates development and improving the techniques of the oil and gas recovery [7] and sequestration of carbon dioxide [8], which, in turn, requires the further comprehension of physics of fluid transport in porous and fractured media.

*corresponding author: kubochkin@ttd.tu-darmstadt.de

†corresponding author: gtatiana@ttd.tu-darmstadt.de

The geometry of the rough, textured and porous media is generally topologically complicated. In mathematical description, the porous media are commonly and easily represented as bundles of capillary tubes [9]. However, angle-containing geometries can serve as a more realistic portrayal of inner structure of those media [10]. A basic element abidingly inherent to all of them is an open wedge-like channel [11–16]. Statics and dynamics of wetting of the wedges (corners) pioneered by works of Taylor and Hauksbee [17] have been studied for decades. One of the first important insights into the liquid behavior inside the wedge has been reported by Concus and Finn [18]. They showed that the steady shape of the liquid interface is only possible when the liquid-gas interface is convex. Thus, a simple geometrical condition $\alpha + \theta_w > \frac{\pi}{2}$, where α is a half of the opening angle of the wedge and θ_w is the contact angle, with which the liquid meets the wall of the wedge (Figure 1), should be fulfilled. Otherwise, when the liquid-gas interface is concave, according to the authors [18], the solution is unbounded and the capillary pressure gradient drives the rivulet along the corner both in the absence of gravity and, against it, when the it is present. Their result has been augmented by consideration of the wedges with the walls having different wetting properties [19]. Besides, the maps for stability in the case of more complicated geometries have been plotted in works [20–23]. In order to derive the Concus-Finn condition, a simplified approach ignoring the actual non-plane liquid interface shape was developed by Berthier et al. [24, 25].

The result of Concus and Finn clearly showed the principal difference between physics of the liquid ascending in round capillary tubes and wedges. Indeed, it is well known that if a vertically oriented capillary tube is brought in contact with a liquid pool ($\theta_w < \frac{\pi}{2}$), the meniscus starts to climb up over the walls of the tube. The maximal height the meniscus can reach is dictated by the gravity and can be evaluated with the Jurin law [14]. Counter-intuitively, if a liquid enters a vertically oriented sharp wedge with the contact angle $\theta_w < \frac{\pi}{2} - \alpha$, gravity cannot stop the ascending rivulet flow, although changes the dynamics of the rivulet propagation. Thus, the rivulet has to propagate infinitely if the wedge is in contact with an infinitely large liquid reservoir. The interface shape in that case is expected to be a hyperbola as was derived in a number of works [26–28]. The predicted infinite rise of the rivulet is obviously caused by infinite curvature of the corner, which is not the case for real systems [28]. Only recently, Gerlach et al. [29] showed that in the real systems, the finite curvature, determined by the manufacturing process, allows the spreading rivulet to stop.

The rivulet flows are omnipresent in the porous and rough media, for which macroscopic considerations of the matter are often insufficient. In order to gain further comprehension of the wetting processes in those media, the nanoscale effects must be incorporated into the models. For the nanoscaled channels, the impact of the surface forces arising from electrostatic, electrodynamic, hydrophobic, steric, and structural interactions is tremendous and cannot be ignored [9]. Despite the fact that there are a number of works on the wetting of wedges employing the surface force approach, all of them aim to discuss either the critical wetting (filling behavior) [30–33] or the stability of rivulets [15]. That leads to consideration of a simplified geometry of the problem (two dimensional instead of three dimensional) and no question on the possible rivulet flow arises since the liquid profile is translationally invariant along the channel. The aforementioned works are of undoubted interest; nevertheless, the problems studied do not allow for the answer whether the surface forces stop the rivulet flow in the case when the Concus-Finn condition is violated, and

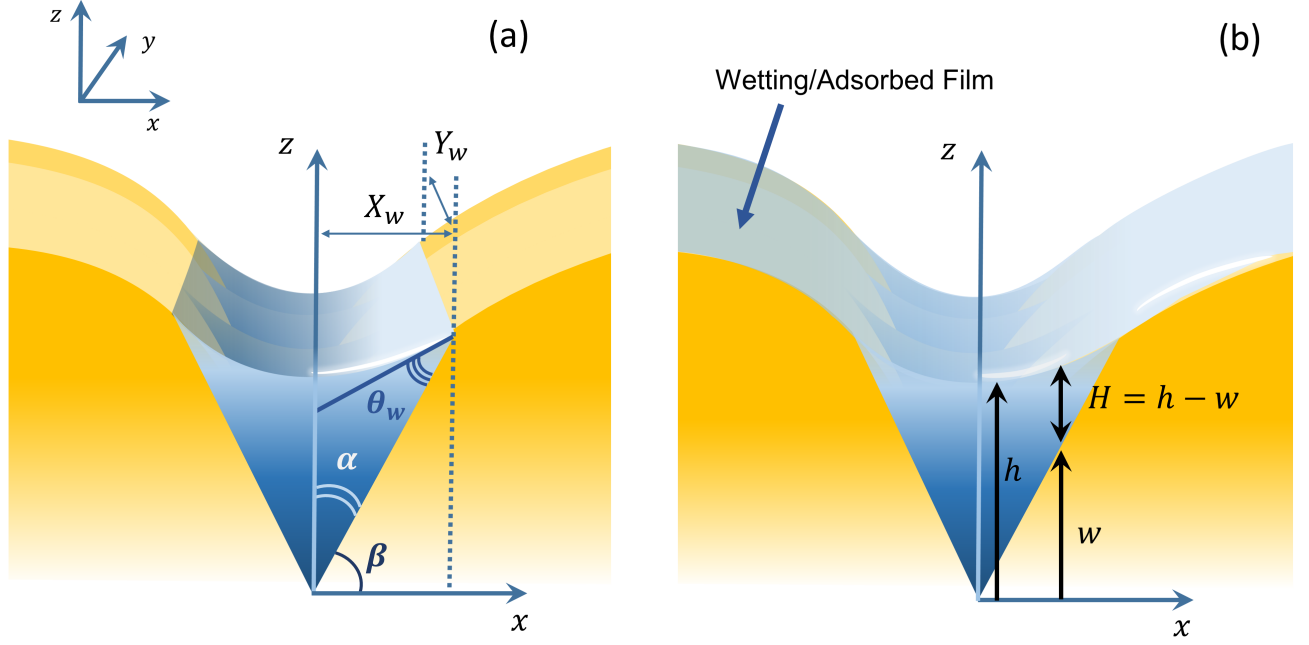


Figure 1: Wetting of the symmetrical wedge channel: (a) the wedge wetted by a liquid within the classical capillarity; no adsorbed film is present. α is the half-opening angle of the wedge, $\beta = \pi/2 - \alpha$ is the angle of inclination of the wedge wall, θ_w is the contact angle, X_w and Y_w are the half-width and length of the wedge, respectively; (b) the wedge wetted by a liquid whose bulk relaxes to the wetting/adsorbed film. Variables h and w measure the distance from the xy -plane to the liquid interface and to the wedge wall, respectively.

what the shape of such a steady rivulet is. Meanwhile, understanding the limits of the applicability of the Concus-Finn condition can significantly help to understand physics of imbibition, since it is directly related to the extent of the liquid front propagation in porous, textured, or fractured materials.

To the best of our knowledge, the only work discussing the stable shapes of the rivulets in the case when the Concus-Finn condition is violated has been performed by Wong et al. [34] for the capillaries with the regular polygon cross-sections. It has been shown by them that accounting for the surface forces renders the existence of the steady-states which are not possible within the classical theory of capillarity. However, the disjoining pressure in their work was used primarily as a mathematical tool in order to resolve the contact line problem.

In the present paper, we study the steady shape of the rivulets in corners/wedges. We demonstrate that introduction of the surface forces embodied in the disjoining pressure leads to the appearance of the steady state of the rivulet in the wedge, although the commonly used Concus-Finn condition is violated. We discuss the influence of the parameters of the disjoining pressure alongside the corner geometry on the steady rivulet profile. Besides, we pay attention to the case when the wedge material is soft and, hence, the wedge walls can be deflected by the traction exerted by the liquid onto the walls of the wedge. The paper is organized as follows. In section 2,

we present the mathematical model and discuss the surface force model. The simulation results for the rivulets in rigid and soft wedges are presented in section 3.

2 Mathematical model

2.1 Governing equations and system parameters

We consider a concave wedge-shaped channel, which is symmetrical with respect to the yz -plane and has a width of $2X_w$ and length of Y_w . The walls of the wedge are chemically and physically homogeneous. They are inclined by angle β with respect to the xy -plane. The opening angle is $2\alpha = \pi - 2\beta$. The variable $h = h(x, y)$ measures the distance between the xy -plane and the position of the liquid interface. The variable $H = h - w$, with $w(x) = |x| \tan \beta$ being the profile of the wall, measures the thickness of the liquid layer inside the wedge. The geometry and the orientation of the wedge are shown in Figure 1. The channel is brought in contact with an infinite reservoir (in practice, it can be a droplet which radius is much larger than the wedge width) located at plane xz the way that a liquid profile $H(x, 0) = I(x)$ at the entrance of the channel is maintained. The wedge is, hence, filled with a liquid of the surface tension γ . The surrounding gas phase contains the vapor of the liquid so it is favorable for the equilibrium adsorbed/wetting film of thickness H_{ads} to form on the walls of the wedge [35, 36]. Wetting films can be introduced as a tool for elimination of the sharp transition between the liquid-gas interface and solid-gas interface. However, in many cases they are present in real systems and affect their behavior drastically [37]. The importance of accounting for the wetting films when considering wetting of nanopores has been also reported recently by Zhang et al. [38].

For the small angles β , the interfacial Hamiltonian of the system given can be written within the gradient-squared approximation as

$$\mathcal{H}[h(x, y)] = \iint \left(\frac{\gamma}{2} |\nabla h|^2 + \int_H^\infty \Pi(\tilde{H}) d\tilde{H} + \Pi(H_{ads}) H \right) dx dy, \quad (1)$$

where the first term is so-called Dirichlet energy, $\Pi(H)$ is the disjoining pressure related to the intermolecular interactions inevitably affecting the behavior of the nanoscale systems and the second integral term is the interfacial potential $\mathfrak{S}(H) = \int_H^\infty \Pi(\tilde{H}) d\tilde{H}$. The last term $\Pi(H_{ads})$ is the Lagrange multiplier. We note again that similar to other works on wedges, we assume small β allows for assumption that thickness of the adsorbed film H_{ads} in the wedge (measured parallel to z -axis as is shown in Figure 1) is equal to that over the planar wall [32, 39]. That leads to the error in the evaluation of H_{ads} which is smaller than 10%, where the error of 10% is reached only in the case of the largest β considered in the present paper.

The disjoining pressure is considered to encompass a non-retarded repulsive van der Waals (London, Debye, Keesom) term and an attractive electrostatic term. It reads $\Pi(H) = \frac{A}{H^3} - K e^{-H/\chi}$ with A, K and χ being the effective Hamaker constant, strength of electrostatic, and Debye-Hückel, respectively. The Hamaker constant reads as $A_h = 6\pi A$. For the sake of simplicity, we assume that the electrostatic component of the disjoining pressure can be taken in a weak overlap approximation [8]. Using the exponential term also allows for going beyond DVLO theory as it is a

fair approximation of the structural (hydration) pressure, which agrees well with the experimental data [40]. In that case, K is the magnitude of the structural disjoining pressure component and χ is the hydration layer thickness [41]. The chosen expression for the disjoining pressure allows to obtain an S-shaped isotherm having both alpha and beta-branches [42] (not to be confused with the inclination angles of the wedge).

If the liquid films are ultrathin ($H < 1\text{nm}$), γ starts to depend on their thickness [43] and can be written in a simplified form as $\gamma(H) = \frac{1}{2} \int_{d_0}^H \hat{\Pi}(\tilde{H}) d\tilde{H}$ with d_0 being the effective cut-off distance and the disjoining pressure $\hat{\Pi}(H)$ resulting from the interactions liquid-vacuum-liquid. The general assumption is that the hydrodynamic framework can still capture the system behavior when the confined region is of $H > 1\text{ nm}$ [8, 38]. Therefore, in the following, we assume that the hydrodynamics approach is still valid and that the surface tension γ is a constant.

The minimization of (1) leads to the Derjaguin equation defining the steady-state shape of the rivulet in the wedge:

$$\nabla^2 H = \frac{\Pi(H_{ads}) - \Pi(H)}{\gamma}. \quad (2)$$

The following boundary conditions have been set: $\frac{\partial H}{\partial x} = -\tan\beta$ at $x = 0$, $H = H_{ads}$ at $x = X_w$, $H = I(x)$ at $y = 0$, and $H = V(x)$ at $y = Y_w$ where the functions $I(x)$ and $V(x)$ for the inlet and limiting profiles, accordingly, are to be defined later. Equation (2) can also be derived from the thin-film equation. We note that setting the wetting film thickness H_{ads} can also be interpreted as exposure of the wedge to the atmosphere of vapor of pressure p_{ads} . That will be discussed later as well.

System	$A \times 10^{21}, \text{J}$	$K \times 10^4, \text{Pa}$	χ, nm	H_1, nm	H_2, nm	$\bar{A} \times 10^6$	$\bar{K} \times 10^2$	$\bar{\chi} \times 10^2$
Case A	2.48	5.25	10.00	4.15	99.43	3.84	7.25	10.06
Case B	2.48	15	5.00	3.79	42.10	19.47	8.76	11.89

Table 1: Parameters of the disjoining pressure isotherms.

In the following, we consider a system consisting of an aqueous phase, a solid hydrophilic phase and a gas phase. We assume that changes of the system's parameters are caused mainly by the changes of electrostatic/structural component of the surface force. In practice, that can be reached, for example, by varying the ionic strength of the aqueous phase. As has been reported, the Hamaker constant varies weakly for aqueous solutions and we keep it, therefore, constant. For the liquid and solid interacting across air, A can be evaluated using the Hamaker constants of corresponding liquid (l) and solid (s) media interacting with themselves across the vacuum (v) as $A_h = \sqrt{A_{h(lvl)} A_{h(svs)}}$ [44]. We set $A_{h(lvl)} = 3.73 \times 10^{-20} \text{J}$, which corresponds to water [8, 44]. For the solid substrate, we choose the Hamaker constant to be $A_{h(svs)} \approx 5.86 \times 10^{-20} \text{J}$, which finally results in $A_h \approx 4.68 \times 10^{-20} \text{J}$ or $A \approx 2.48 \times 10^{-21} \text{J}$. The disjoining pressure parameters for two cases – case A and case B – are presented in Table 1. The corresponding disjoining pressure

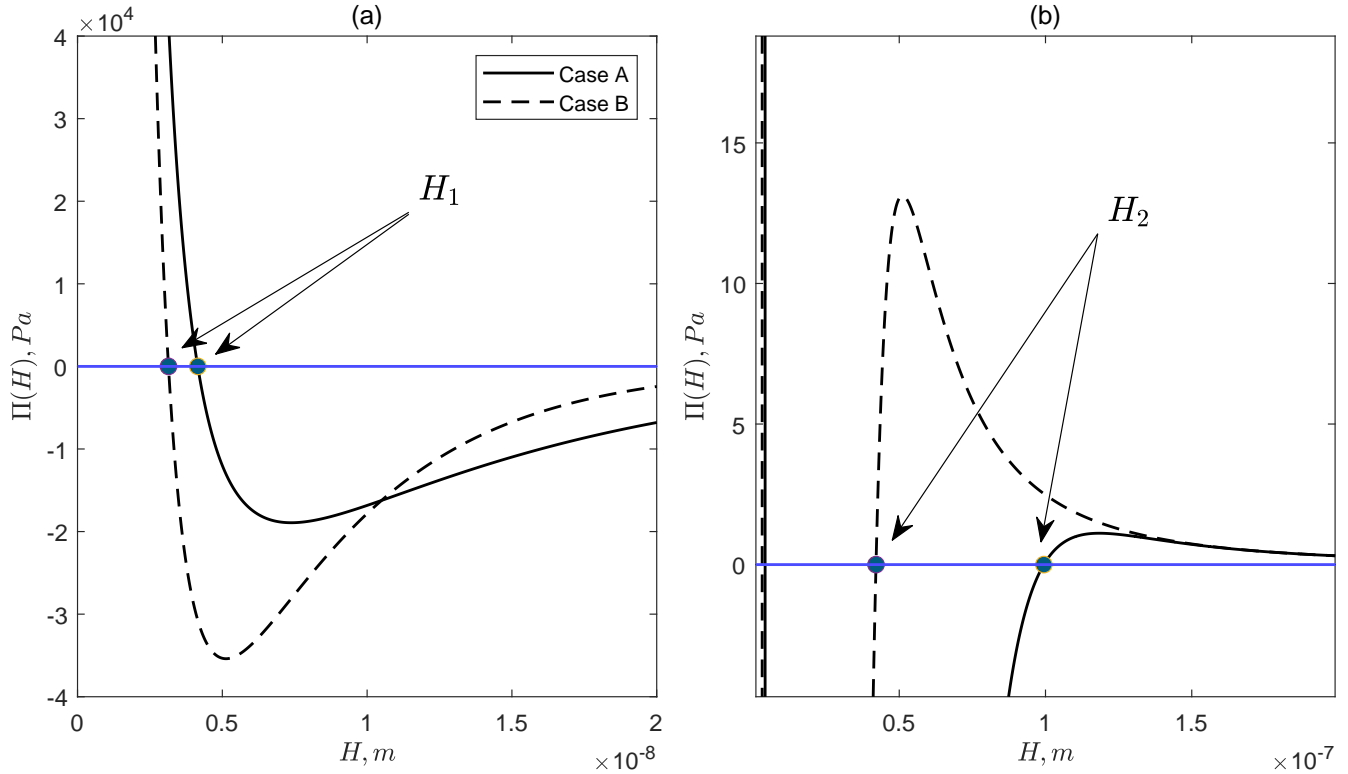


Figure 2: Disjoining pressure isotherms used in the present work (Table 1): (a) disjoining-conjoining pressure transition defining H_1 ; (b) conjoining-disjoining pressure transition defining H_2 .

isotherms are shown in Figure 2(a,b). In contrast to the sessile droplets, the van der Waals forces alone still allow for the equilibrium wetting film existence. The difference between cases $A \neq 0, K = 0$ and $A \neq 0, K \neq 0$ is expected only for relatively thick alpha-films.

Wetting behavior of a system is known to be interrelated with the interfacial potential/disjoining pressure isotherms. Employing the Frumkin-Derjaguin theory [45], the equilibrium contact angle of the liquid meeting the surface covered with the adsorbed film can be evaluated as

$$\cos \theta_w = 1 + \frac{1}{\gamma} \int_{H_1}^{\infty} \Pi(H) dH = 1 + \frac{\mathfrak{S}(H_1)}{\gamma} \quad (3)$$

where $H_1 = -3\chi\mathcal{W}_0\left(-\frac{A^{1/3}}{3K^{1/3}\chi}\right)$ is the first root of equation $\Pi(H) = 0$ written with the use of the Lambert \mathcal{W} -function (see Supplementary Material), and $\mathfrak{S}(H_1)$ defines the minimum of the interfacial potential. For both isotherms presented, the contact angle is $\theta_w \approx 5^\circ$. This contact angle can be observed for a macroscopic meniscus. As can be seen from equation (3), keeping the contact angle θ_w constant means preserving the minimal value of the interfacial potential while allowing for the variations of its shape. The Hamaker constant $A_{h(svs)}$ presented above is a value adjusted to meet the chosen θ_w . Nevertheless, it is still very close to $A_{h(svs)}$ corresponding to mineral surfaces [8] or a polymer surface such as rubber [46].

Before the solution, equation (2) is written in a dimensionless form using the following dimensionless variables: $\bar{x} = x/H_2$, $\bar{y} = y/H_2$, $\bar{H} = H/H_2$, $\bar{\Pi}(\bar{H}) = \Pi(H)H_2/\gamma$ with $H_2 =$

$-3\chi\mathcal{W}_{-1}\left(-\frac{A^{1/3}}{3K^{1/3}\chi}\right)$ being the second root of equation $\Pi(H) = 0$ (see Figure 2, b). Since generally the amplitude of the attractive (conjoining the interfaces) forces is much stronger than those repulsive (Figure 2, a-b), choosing H_2 for the role of the scaling parameter defining the range of the surface force action is natural. The dimensional width of the wedge was $X_w = 700$ nm and was scaled with respect to the H_2 of the isotherm chosen. The dimensional length was $Y_w > 500$ nm and, analogically, was scaled with respect to the H_2 of the isotherm chosen. The equation for the equilibrium shape of the rivulet in the dimensionless form is:

$$\nabla^2 \bar{H} = \bar{\Pi}(\bar{H}_{ads}) - \bar{\Pi}(\bar{H}). \quad (4)$$

The equation (4) is solved numerically using finite element analysis. It has been checked that the solution converges as maximal element size decreases. It has been checked additionally that the variation of \bar{Y}_w as well as the number of points, over which the solution has been interpolated, led to only small (less than 2%) differences in a decay length \bar{D}_{cr} (for the definition of \bar{D}_{cr} , see subsection 3.1).

2.2 Inlet profile and the limiting profile of the rivulet

As we stated before, we assume that at the inlet $\bar{y} = 0$, the wedge is connected to the reservoir of infinite volume and the profile of the liquid-gas interface $\bar{h}(\bar{x}, 0) = \bar{I}(\bar{x}) + |\bar{x}| \tan \beta$ does not change in time. In real-life systems that can be a nanopore with a macroscopic droplet at its entrance. Assuming that at the entrance, away from the wall of the channel, the shape of the interface $\bar{I}(\bar{x})$ can be obtained from the macroscopic considerations, one can employ the Young-Laplace equation. One integrates it twice and obtain $\bar{h}(\bar{x}) = \frac{\tan(\beta - \theta_w)(\bar{x}^2 - \bar{X}_w^2)}{2\bar{X}_w} + \bar{H}_{ads}$. Since the inlet profile must satisfy the boundary conditions and also relax to the wetting film, we introduce a coordinate \bar{x}_t of the point, where the macroscopic meniscus meets the wetting film with the contact angle θ_w . The inlet profile is, hence, a piece-wise function defined as

$$\bar{h}(\bar{x}) = \begin{cases} \frac{\tan(\beta - \theta_w)(\bar{x}^2 - \bar{x}_t^2)}{2\bar{x}_t} + \bar{x}_t \tan \beta + \bar{H}_{ads} + c_1 \bar{H}_{ads}, & \text{if } \bar{x} < \bar{x}_t. \\ \bar{H}_{ads}, & \text{if } \bar{x} > \bar{x}_t + c_2 (\bar{X}_w - \bar{x}_t). \end{cases} \quad (5)$$

The value of \bar{x}_t has been kept equal to $\bar{x}_t = 0.95\bar{X}_w$, unless other is stated (see also Supplementary Materials). Real constants c_1 and c_2 are chosen in a way to allow for a smooth transition from the profile to the wetting film. The constant c_2 allowed to change the width of the transition region without changes in $\bar{I}(0)$. Two regions – the macroscopic profile and the film – have been matched (see Supplementary material). Spline interpolation showed overshoots and undulations in the transition region. Therefore, piece-wise cubic Hermite polynomials have been used. Giving less smooth transition zones, it nevertheless allowed to minimize the undesirable waviness there.

The function $H(\bar{x}, \bar{Y}_w) = \bar{V}(\bar{x})$ describes the interface shape far away from the inlet. This function is unknown a priori. Far away from the inlet, the interface is translationally invariant

along the Y -axis. In that case, the reduced one-dimensional Hamiltonian $\mathcal{H}[h(x)]$ can be written and the liquid profile, hence, can be evaluated using one-dimensional Derjaguin equation

$$\frac{d^2 \bar{H}}{d\bar{x}^2} = \bar{\Pi}(\bar{H}_{ads}) - \bar{\Pi}(\bar{H}), \quad (6)$$

which solution reads

$$\int_{\bar{H}_{ads}}^{\bar{H}} \frac{d\hat{H}}{\sqrt{2 \int_{\bar{H}_{ads}}^{\hat{H}} (\bar{\Pi}(\bar{H}_{ads}) - \bar{\Pi}(\hat{H})) d\hat{H}}} = \bar{x}_{ads} - \bar{x}. \quad (7)$$

We introduce the limiting thickness of the interface at $\bar{x} = 0$: $\bar{H}_w = \bar{V}(0)$. The value of \bar{H}_w depends on the disjoining pressure and on the slope of the wall as follows from the equation

$$\frac{\tan^2 \beta}{2} = \bar{\Pi}(\bar{H}_{ads}) (\bar{H}_w - \bar{H}_{ads}) - \int_{\bar{H}_{ads}}^{\bar{H}_w} (\bar{\Pi}(\bar{H})) d\bar{H}. \quad (8)$$

As long as the disjoining pressure isotherm contains the exponential tail, the equation (8) is transcendental and the integral in (7) cannot be taken analytically. Therefore, equations (7) and (8) were integrated numerically, subject to boundary conditions $\bar{H} = \bar{H}_{ads}$ at $\bar{x} = \bar{x}_w$ and $\frac{d\bar{H}}{d\bar{x}} = \tan \beta$ at $\bar{x} = 0$. In order to avoid a singularity when the adsorbed film thickness is reached, the integration was started from $\bar{H}_{ads} + \epsilon$ where for ϵ the condition $\epsilon/\bar{H}_{ads} \ll 1$ is fulfilled. The function $V(x)$ was obtained as $V(x) = \bar{H}(\bar{x}) + |x| \tan \beta$. The solution of (6) has been checked by the direct differentiation as well as by solving it as a boundary value problem fully numerically.

When the wetting film is very thin: $\bar{H}_{ads} = \phi \bar{H}_1$ with $\phi \ll 1$, one can expect the limiting height of the rivulet \bar{H}_w to be smaller than the height $\bar{H}_{c1} = -4\bar{\chi}\mathcal{W}_0 \left(-\frac{(3\bar{A})^{1/4}}{4\bar{K}^{1/4}\bar{\chi}^{3/4}} \right)$, where the disjoining pressure isotherm finds its minimum. In this case, the disjoining pressure isotherm can be linearized and equation (8) can be easily solved analytically. The limiting height \bar{H}_w can be obtained as

$$\bar{H}_w = \bar{H}_{ads} + \tan \beta \sqrt{\frac{\bar{H}_1 - \bar{H}_{ads}}{\bar{\Pi}(\bar{H}_{ads})}} \quad (9)$$

The derivation and discussion of (5) and (9) are presented in Supplementary Materials.

3 Results and discussion

3.1 Rigid Wedges

The presence of the surface forces stabilizing the adsorbed/wetting film allows for the steady state meniscus in the wedge even when the Concus-Finn condition is not fulfilled. The solution of equation (4) for the adsorbed film thicknesses $\bar{H}_{ads} = 0.0125$, ($\phi = 0.3$) and $\bar{H}_{ads} = 0.0334$,

($\phi = 0.8$) are illustrated in Figure 3. The thickness of the liquid layer \bar{H} and the liquid-gas interface \bar{h} are shown in Figure 3(a, b) and (c, d), correspondingly. As is set by the boundary conditions, the thickness of the liquid layer is maximal at the entrance of the wedge. The liquid layer thickness at the plane $\bar{x} = 0$ decays until the limiting thickness \bar{H}_w dictated by the solution of equation (8) is reached. One can see that when the adsorbed film is thinner (Figure 3, a, c), the thickness of the liquid filling the wedge diminishes down to the limiting profile $\bar{V}(\bar{x})$ very close to the entrance (schematically shown by the arrows). In contrast to that, when the adsorbed film is thicker (Figure 3, b, d), the liquid thickness decreases gradually and reaches the limiting profile $\bar{V}(\bar{x})$ far away from the entrance.

The smoothness of the transition from the inlet to the limiting profile can be illustrated more clear by plotting the thickness \bar{H} of the liquid layer at $\bar{x} = 0$ (Figure 4, a). We quantify this transition by introducing the decay length \bar{D}_{cr} . We define \bar{D}_{cr} as the length, at which the relative difference between $\bar{H}(0, \bar{y})$ and \bar{H}_w is less than 1%. The decay length is shown in Figure 4(a) by the black arrows and squared markers. The calculated values of \bar{D}_{cr} are presented in Figure 4(b). One can see that \bar{D}_{cr} increases with the increasing ratio ϕ (increasing \bar{H}_{ads}). The observed trend is obviously related to changes in the limiting profile $\bar{V}(\bar{x})$ of the rivulet resulting from equation (6). The limiting profile is in turn dictated by interplay of curvature-induced and disjoining pressures. In Figure 4(c-d), the limiting rivulet profiles as well as the dependency of the dimensionless curvature $\bar{\kappa}_w = \frac{\partial^2 \bar{H}}{\partial \bar{x}^2}(0, \bar{Y}_w)$ and dimensionless limiting height of the rivulet $\bar{H}_w = \bar{V}(0)$ on the ratio ϕ are shown. The limiting height increases as the adsorbed film \bar{H}_{ads} increases, while the opposite trend is observed for the dimensionless curvature: it decreases with the increasing \bar{H}_{ads} . In Figure 5, decay length \bar{D}_{cr} is plotted against the limiting height \bar{H}_w . As the adsorbed/wetting film thickness increases causing a rise of \bar{H}_w , the decaying length \bar{D}_{cr} increases as well.

As has been briefly mentioned before, the adsorbed/wetting film of a constant equilibrium thickness \bar{H}_{ads} is formed on the walls of the wedge when it is exposed to the vapor atmosphere of pressure \bar{p}_{ads} . The value of the corresponding vapor pressure or relative humidity $RH = \frac{\bar{p}_{ads}}{p_s}$ (where p_s is the pressure of the saturated vapor) can be calculated using Derjaguin-Churaev-Müller theory of the surface forces [35]:

$$RH = \exp\left(-\frac{\nu_m \Pi(H_{ads})}{RT}\right) \quad (10)$$

where ν_m is a molar volume of liquid, R is a gas constant, T is temperature. We plot the dependence of ϕ on RH in Figure 6. One can see that very thin wetting films can exist even when humidity is close to zero. The isothermal increase of the relative humidity RH leads to the increasing limiting height \bar{H}_w and, therefore, to the increasing decay length \bar{D}_{cr} of the rivulet.

The rivulet shape is drastically affected by the geometry of the wedge as well. In order to show that, we solve equation (4) for five different inclination angles β chosen in the way that the steady liquid profile in the sense of the Concus-Finn consideration does not exist. The ratio β/θ_w varies from 1 to 5.

In Figure 7(a), the liquid profiles corresponding to different inclination angles β (ratios β/θ_w) are presented. Here, we first consider the case when increasing β leads to increasing of the maximal film thickness at the inlet. That naturally follows from inlet condition (5) with \bar{x}_t kept constant.

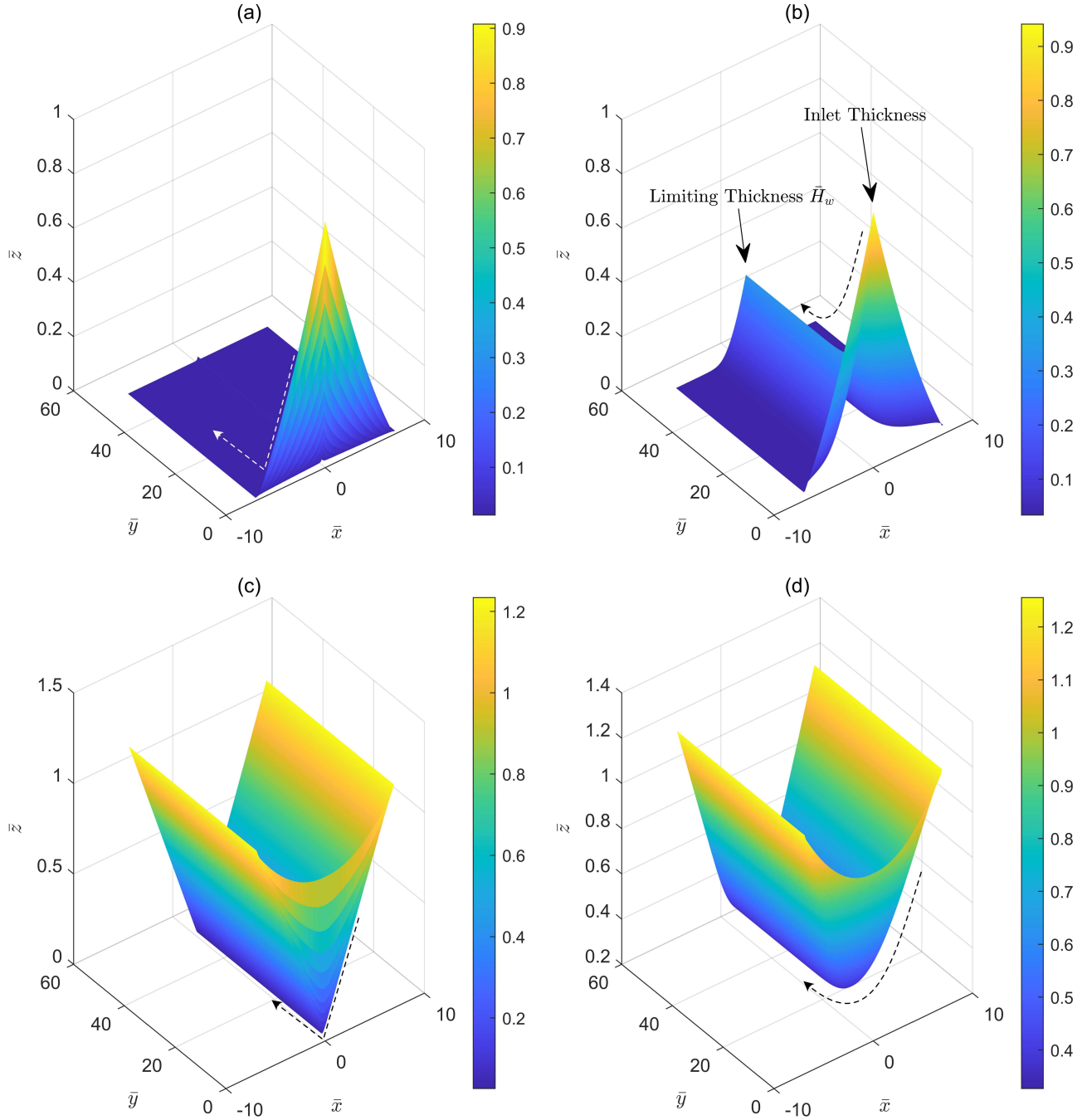


Figure 3: Wetting of the symmetrical wedge-shaped channel. The thickness of the liquid \bar{H} in the channel when the equilibrium adsorbed film thickness (a) $H_{ads} = 0.0125$ ($\phi = 0.3$) and (b) $H_{ads} = 0.0334$ ($\phi = 0.8$). The profile of the liquid-gas interface \bar{h} in the channel when the equilibrium adsorbed film thickness (c) $H_{ads} = 0.0125$ ($\phi = 0.3$) and (d) $H_{ads} = 0.0334$ ($\phi = 0.8$). The inclination angle is $\beta = 2\theta_w$. The isotherm A has been used for the calculations. The color bars are to show the thickness/height distribution. Less number of points than the solutions contain was used for plotting in order to decrease rendering time and avoid low-level graphic errors.

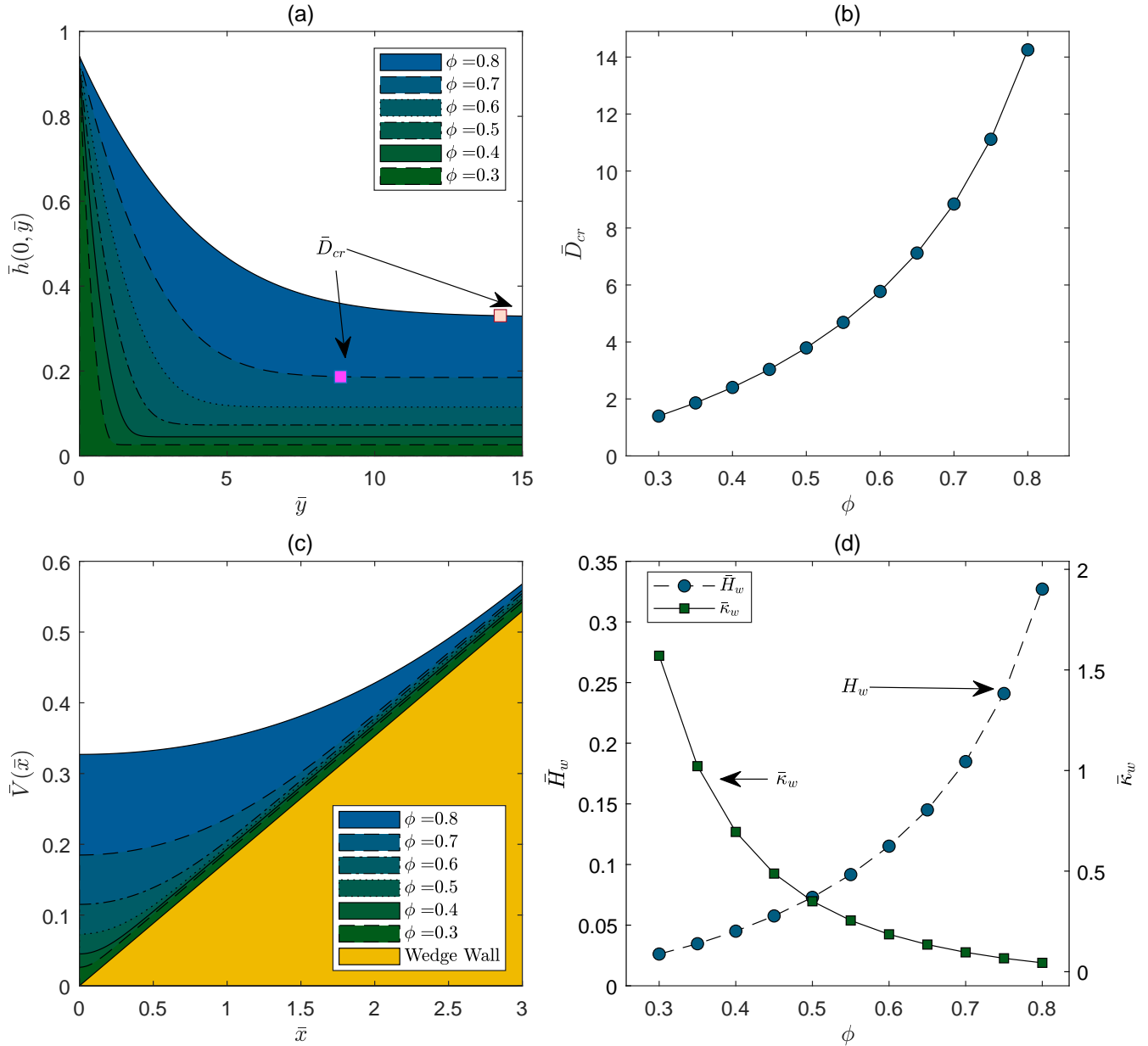


Figure 4: Wetting of the wedge channel; (a) thickness of the rivulet at the symmetry axis ($\bar{x} = 0$) calculated with the different adsorbed film thicknesses \bar{H}_{ads} ; (b) dependence of the decay length \bar{D}_{cr} on the adsorbed film thickness; the decay lengths are illustrated in (a); (c) limiting profiles $\bar{V}(\bar{x})$ of the rivulets calculated with the different adsorbed film thicknesses \bar{H}_{ads} ; (d) dependence of the limiting curvature $\bar{\kappa}_w$ and limiting height \bar{H}_w of the rivulet at the symmetry axis ($\bar{x} = 0$) on the adsorbed film thickness (or parameter ϕ). The inclination angle is $\beta = 2\theta_w$. The system behavior is defined by the isotherm A. The lines in (b) and (d) are to guide an eye.

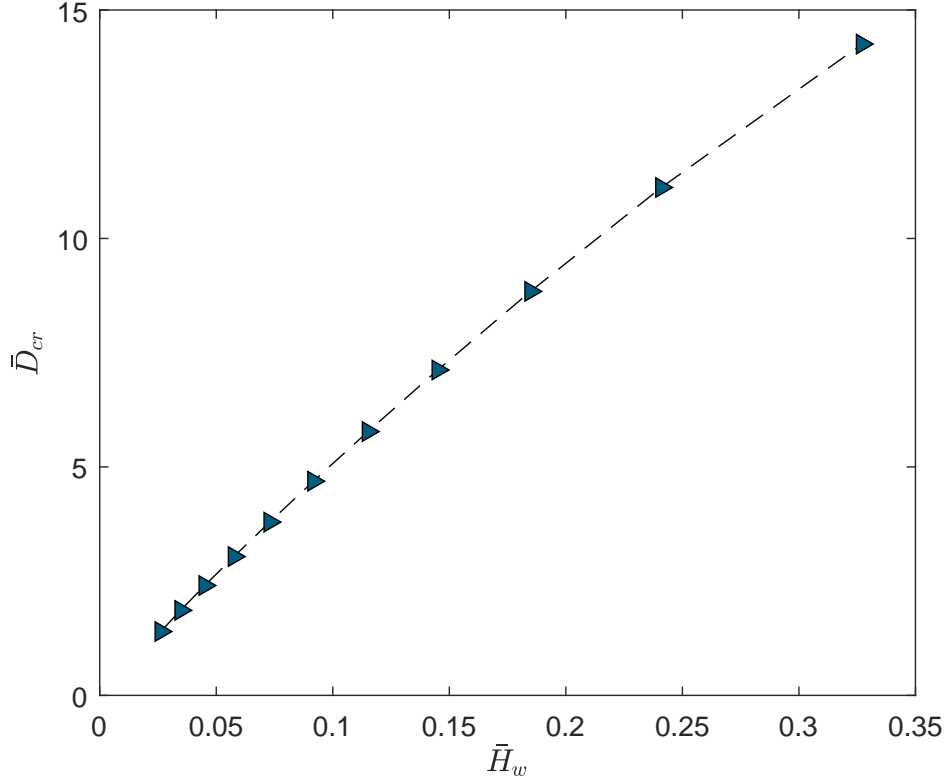


Figure 5: Dependence of the decay length \bar{D}_{cr} on the limiting thickness \bar{H}_w of the profile $\bar{V}(\bar{x})$. The inclination angle is $\beta = 2\theta_w$. The system behavior is defined by the isotherm A.

Interestingly, when closing the wedge in a described way, the decay length of the rivulet \bar{D}_{cr} increases linearly with β (Figure 7, b). In contrast to that, the dependence of the limiting height of the rivulet \bar{H}_w on the ratio of the wedge inclination angle β and contact angle θ_w demonstrates the non-linear growth (Figure 7, c). The dependencies $\bar{H}_w(\beta)$ are plotted in Figure 7(c) for different values of ϕ . It can be seen that when the wetting film is thin, the effect of the the wedge inclination is not strong, while it becomes more pronounced when the adsorbed film is thicker (RH is higher). It is shown in Figure 5 that the decay length \bar{D}_{cr} increases with the increasing \bar{H}_w . Therefore, one should expect \bar{D}_{cr} is more significantly affected by the wedge angle when the adsorbed film is thicker (RH is higher). In Figure 7(d), the decay length \bar{D}_{cr} is plotted against ϕ for different ratios β/θ_w and the expected trend can be observed.

As has been stated afore and shown in Figure 7(a), the thickness of the liquid layer at the center of the inlet $\bar{I}(0)$ has not been preserved when closing the wedge (increasing wedge angle β). The variation of $\bar{I}(0)$ can affect the dependence $\bar{D}_{cr}(\beta)$. In order to eliminate the effect of $\bar{I}(0)$ on $D_{cr}(\beta)$, we perform calculations, in which β has been varied, while $\bar{I}(0)$ is kept constant. The latter was possible by varying the value of \bar{x}_t from $\approx 0.29\bar{X}_w$ ($\beta = 5\theta$) to $\approx 0.95\bar{X}_w$ ($\beta = \theta$). The values of \bar{x}_t as well as of the parameters c_1 and c_2 of the inlet profiles are given in Supplementary materials. The inlet profiles $\bar{I}(\bar{x})$ employed are shown in Figure 8(a). The resulting thicknesses of the rivulets along the symmetry axis of the wedge are presented in Figure 8(b). Despite the fact that $\bar{I}(0)$ is now the same, the rivulet in the wedge, where the wetting/adsorbed film is thicker, still extends over the longer distance. The dependencies of \bar{D}_{cr} on β/θ_w for the cases of both same

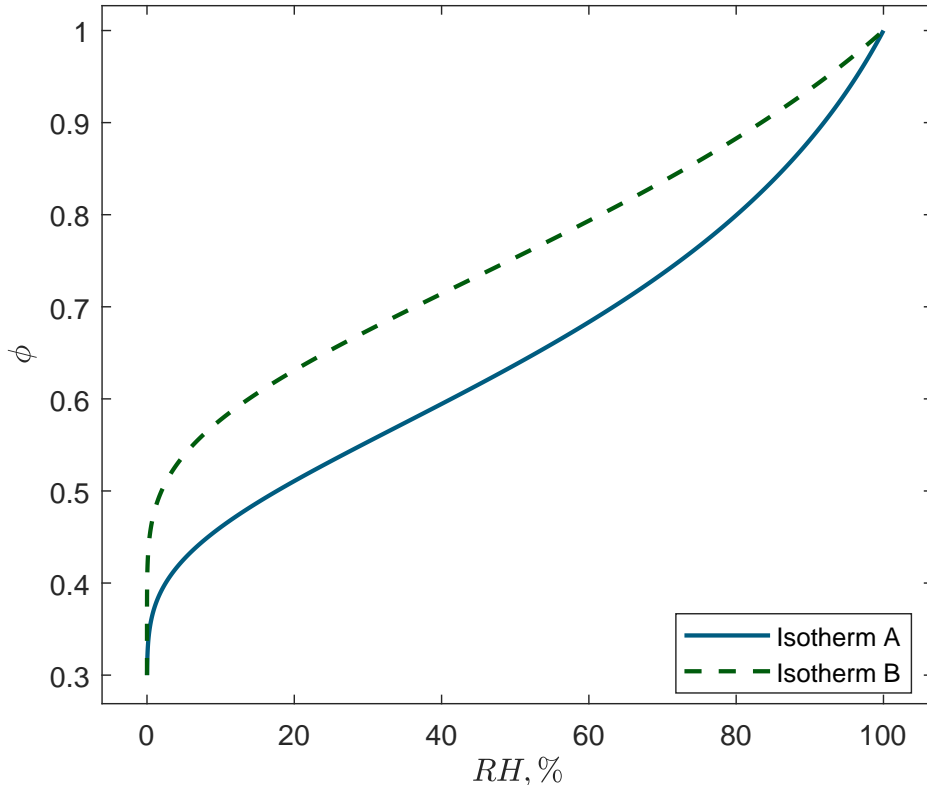


Figure 6: Influence of the relative humidity on the thickness of the adsorbed/wetting film at $T = 293$ K ($\nu_m = 18 \times 10^{-3}$ kg/m) for isotherms A and B.

and different $\bar{I}(0)$ are shown in Figure 8(c). Keeping thickness of the rivulet at the inlet $\bar{I}(0)$ constant does not break the linear dependence of \bar{D}_{cr} on β/θ_w , although makes it less pronounced.

According to the Washburn law, the extent of the liquid front in the porous media is related to the size of the pores [9]. Moreover, the kinetics of the liquid front in corner geometry depends on the meniscus height at the inlet [16]. Therefore, it is also of interest to study how the size of the wedge affects the decay length \bar{D}_{cr} of the static rivulet. The width of the wedge was varied from $\bar{X}_w \approx 7$ to $\bar{X}_w \approx 28$, the length of the wedge \bar{Y}_w , the adsorbed film thickness \bar{H}_{ads} , and the wedge inclination angle β were kept constant. The profiles of the liquid $\bar{h}(\bar{y})$ filling corresponding wedges are presented in Figure 9. In the larger wedges, the liquid thickness at the inlet is larger and the rivulet extends along a larger distance. Therefore, the decay length \bar{D}_{cr} increases with increasing size of the wedge. All the rivulets have been initially computed with the inlet located at $\bar{y} = 0$. However, the shape of the profiles can give us an idea that $\bar{h}(\bar{y})$ being plotted and shifted along \bar{y} with respect to the profile of the liquid in the widest wedge might match. Indeed, $\bar{h}(\bar{y})$ for the wedges with the widths of up to fourfold difference coincide almost perfectly when plotted with a subsequent shift (Figure 9). That observation can be of significant help when a profile of a liquid rivulet is known for a large angular pore and the length of a smaller rivulet is to be evaluated.

As can be expected, the shape of the rivulet will be different for different liquid systems. It is, however, of substantial interest how the surface forces affect the steady state of nanorivulets in the systems having the same macroscopic wetting behavior (same θ_w and $\bar{\mathfrak{S}}(\bar{H}_1)$). In the following, we show how the disjoining pressure isotherm influences the shape of the meniscus in the wedge.

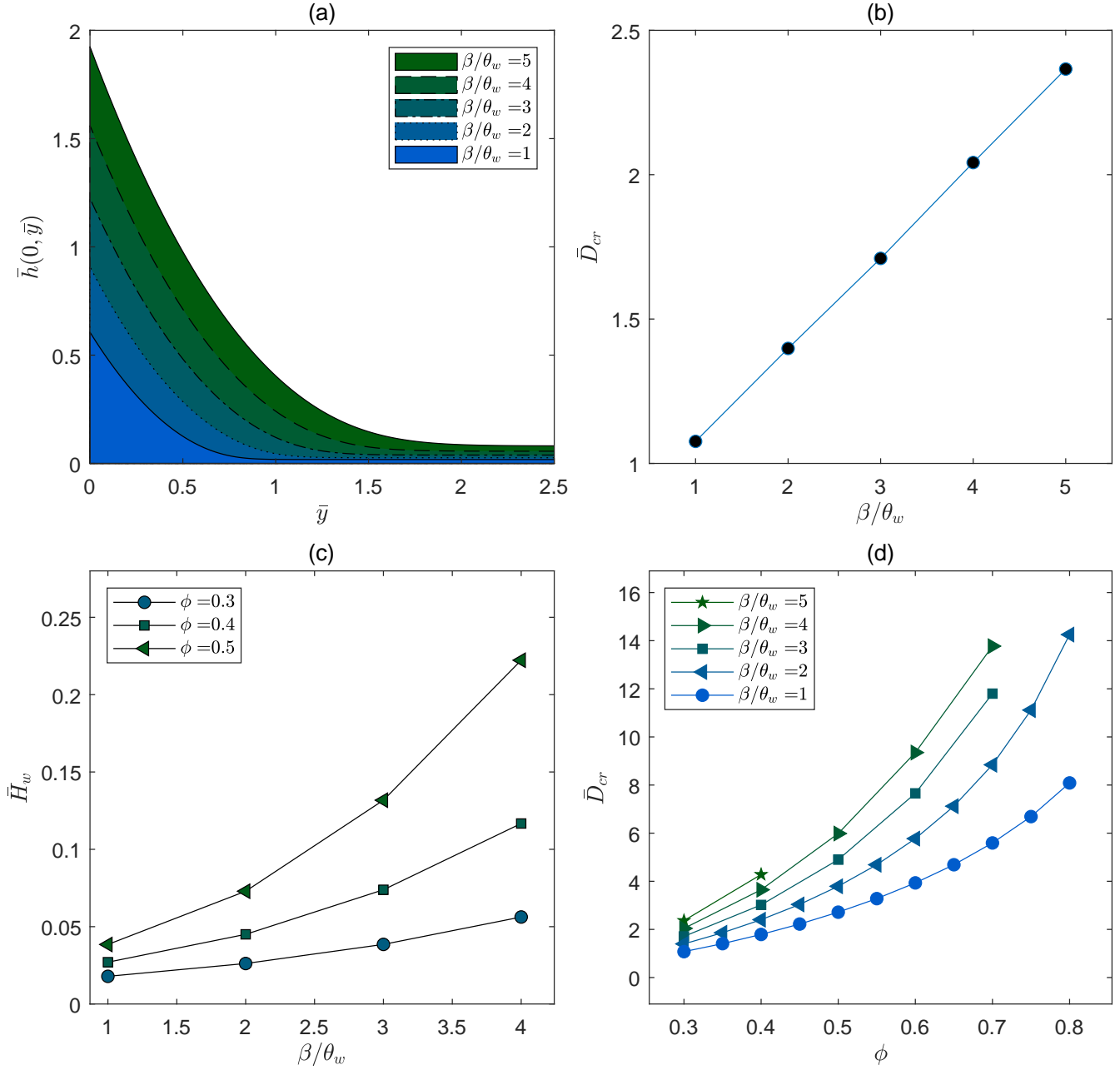


Figure 7: Wetting of the wedges with different inclination angle β : (a) thickness of the liquid layer at the symmetry axis ($\bar{x} = 0$) calculated with the different inclination angles β ($\phi = 0.3$); (b) influence of the inclination angle β on the decay length \bar{D}_{cr} ; (c) influence of the inclination angle β on the limiting thickness \bar{H}_w of the profile $\bar{V}(\bar{x})$ for different ϕ ; (d) influence of the ratio ϕ (adsorbed film thickness) on the decay length \bar{D}_{cr} for wedges with the walls inclined by different angles β . The system behavior is defined by the isotherm A.

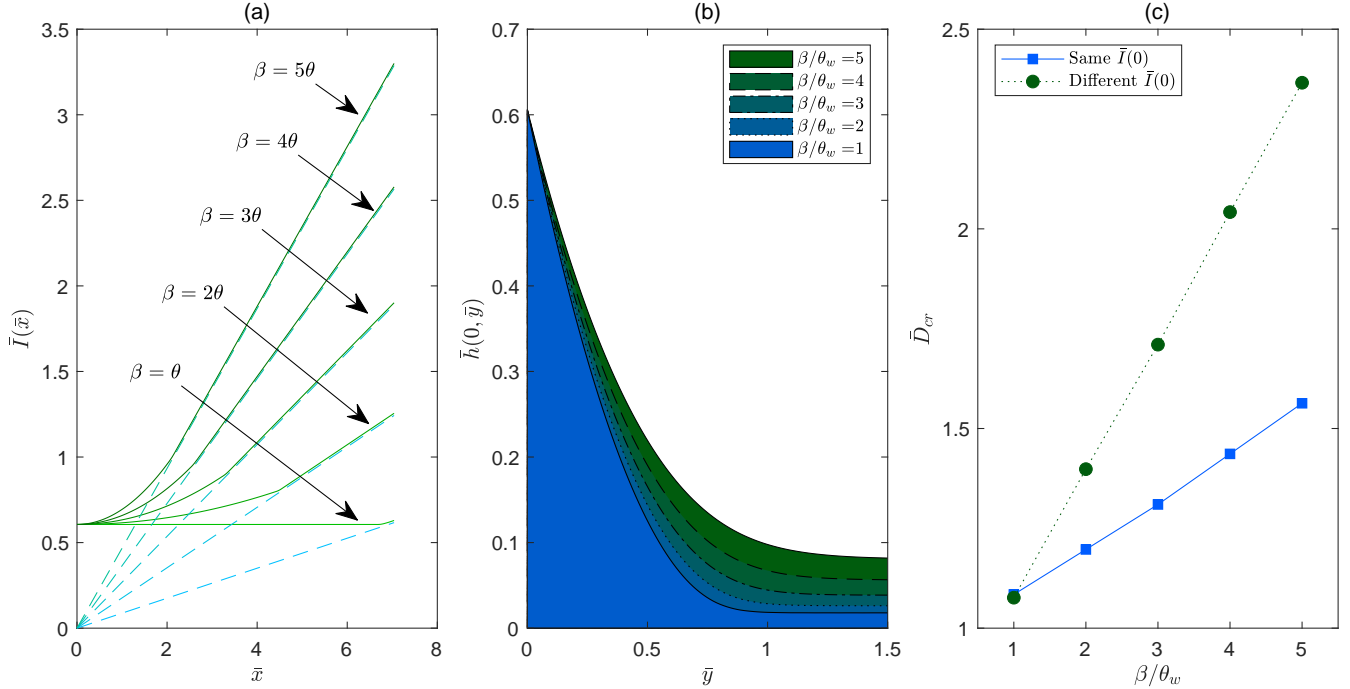


Figure 8: Wetting of the wedges with the different inclination angles β : (a) inlet profiles $\bar{I}(\bar{x})$ for different inclination angles β ($\phi = 0.3$). The thickness of the liquid layer at the inlet, at the symmetry axis ($\bar{x} = 0$) is fixed; (b) thickness of the liquid layer at the symmetry axis ($\bar{x} = 0$) calculated with the different inclination angles β ($\phi = 0.3$); (c) influence of the inclination angle β on the decay length \bar{D}_{cr} . The system behavior is defined by the isotherm A.

Two isotherms shown in Figure 2 have been employed. We note that dimensional values of H_{ads} for isotherm B were smaller than 1nm. However, evaluation of the surface tension according to [47] accounting for the hydrogen bonds of water [48] shows that its alteration does not exceed 1.5%. Therefore, the assumption of the constant surface tension is still valid.

In Figure 10(a), the limiting profiles $\bar{V}(\bar{x})$ are shown for both isotherms. Despite the fact that the contact angle θ_w is preserved, at the nanoscale, the limiting profiles demonstrate significant differences in the limiting heights \bar{H}_w . That is caused by the interplay of long-range and short-range surface forces. Since wedges of the same \bar{X}_w , \bar{Y}_w , \bar{H}_{ads} and β are under consideration, limiting height \bar{H}_w is the main parameter impacting the decay length (Figure 10, b). The influence of the disjoining pressure isotherm on \bar{H}_w can be understood from the simplified consideration based on (9). Since \bar{H}_{ads} are the chosen to be the same for both wedges, the differences in the limiting height \bar{H}_w are mainly rendered by the value of $\bar{\Pi}(\bar{H}_{ads})$ which is larger for the isotherm B. The latter causes smaller \bar{H}_w . The same can also be comprehended in a more graphical way – namely, considering the slope of the alpha-branch of the disjoining pressure isotherm (see Supplementary Material). Since the values of \bar{H}_w are much smaller for the case of isotherm B, the rivulet is forced to reach the limiting profile very close to the inlet (Figure 10, c) and has smaller values of \bar{D}_{cr} , as is shown in Figure 10(d). Thus, tuning the parameters of the disjoining pressure isotherm can be a way for control of the length, over which the rivulets can extend. Similarly to the trend observed for influence of the inclination angles, the differences between \bar{H}_w and \bar{D}_{cr} for isotherms A and B

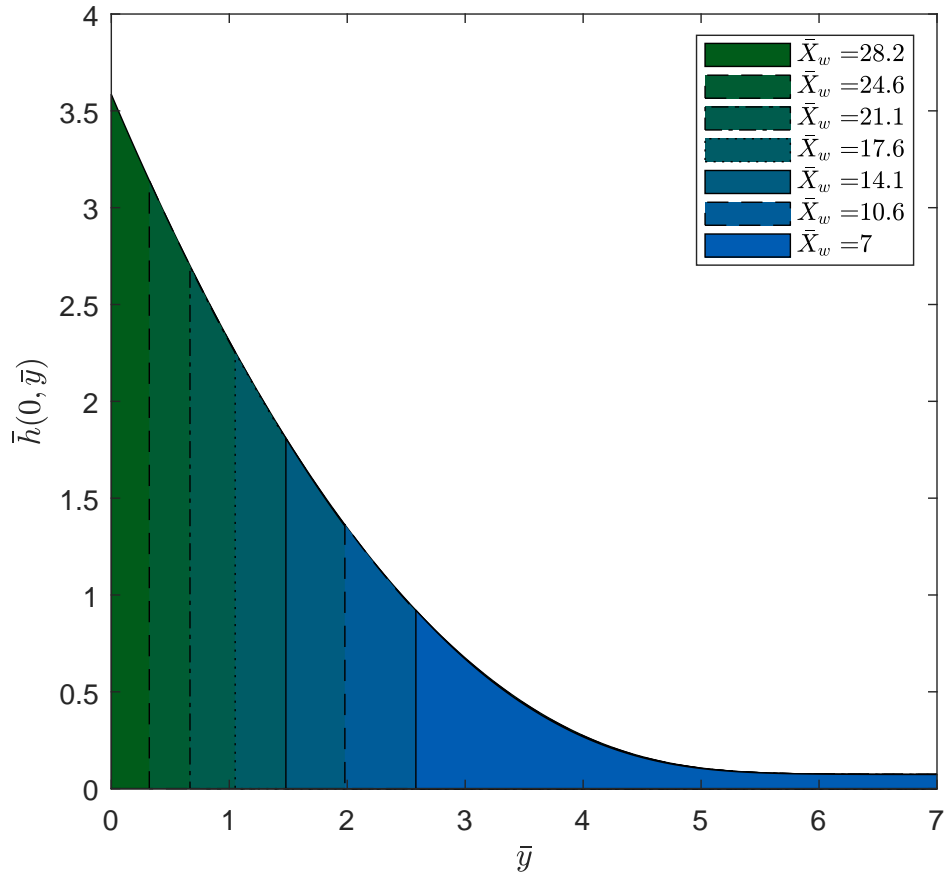


Figure 9: Wetting of the wedges of different size: Thickness of the rivulets at the symmetry axis ($\bar{x} = 0$). The inclination angle is $\beta = 2\theta_w$. The system behavior is defined by the isotherm A.

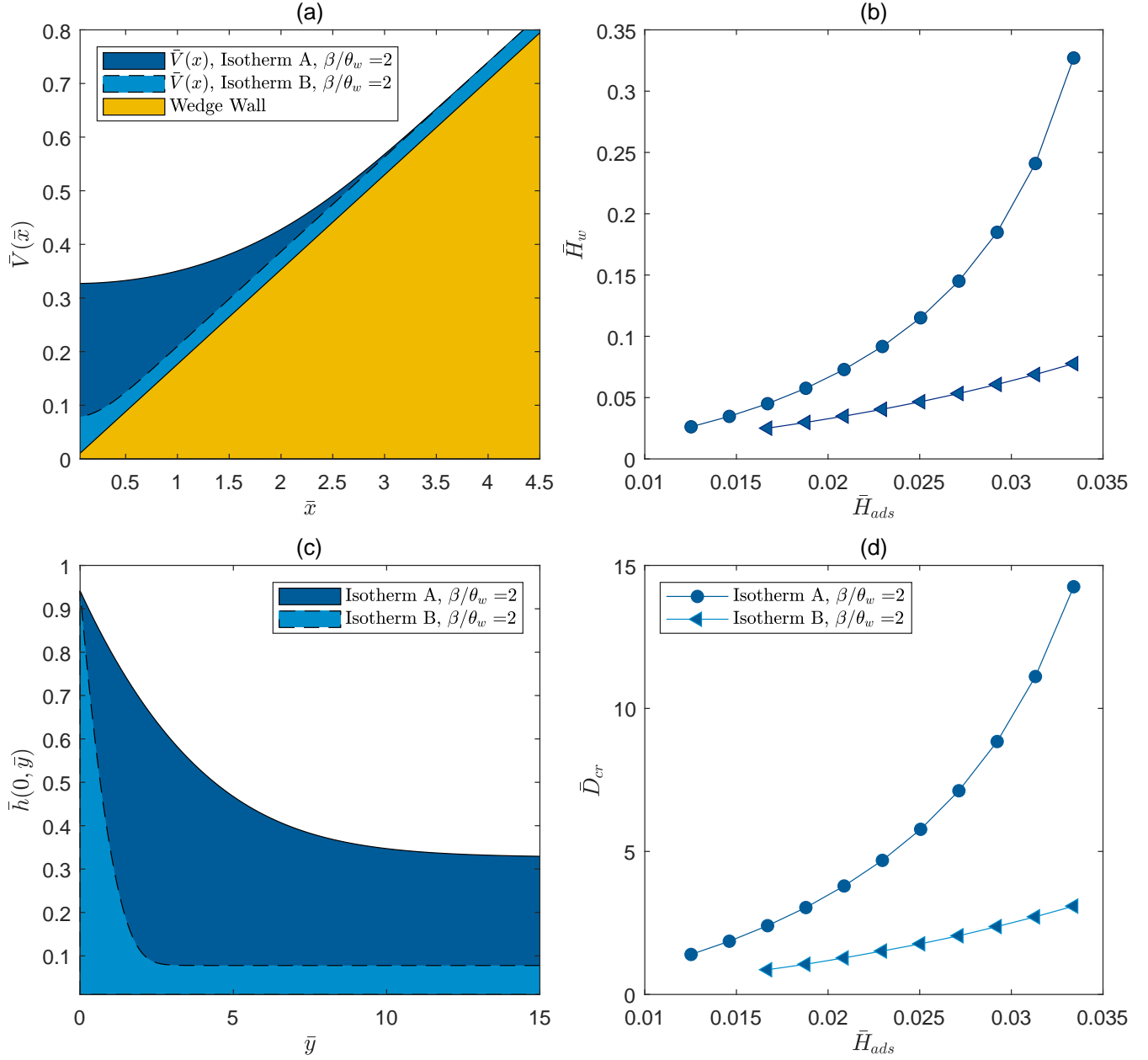


Figure 10: Influence of the disjoining pressure on the wetting of the wedge; (a) limiting profiles $\bar{V}(\bar{x})$ of the rivulets calculated with the adsorbed film thicknesses $\bar{H}_{ads} = 0.0334$; (b) dependence of the limiting height \bar{H}_w on the adsorbed film thickness; (c) thickness of the rivulet at the symmetry axis ($\bar{x} = 0$) calculated with the adsorbed film thicknesses $\bar{H}_{ads} = 0.0334$; (d) dependence of the decay length \bar{D}_{cr} on the adsorbed film thickness. The inclination angle is $\beta = 2\theta_w$. The lines in (b) and (d) are to guide an eye.

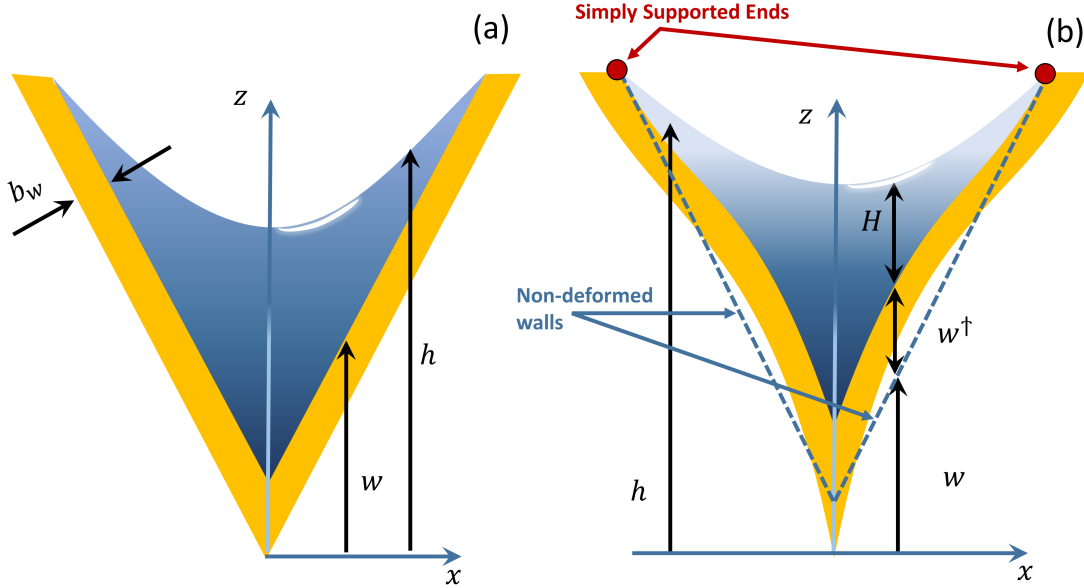


Figure 11: Schematic illustration of (a) wedge with rigid walls and (b) wedge with deformable walls. The position of the liquid-gas interface is h , the position of the undeformed wall and deformed wall is w and w^\dagger , accordingly. Thickness of the liquid rivulet filling the wedge is H .

are larger when the adsorbed film is thicker (humidity is higher).

3.2 Soft wedges

In many cases, surfaces, which are in contact with liquid, can respond to its action by deformation, dissolution, or swelling [41]. Understanding of possible bending/folding of solid structures is of utmost importance in different branches of industry such as micro- and nanofabrication [49]. Shrinkage of cement-based materials when drying also lacks understanding, which is paramount for its quality improvement and control [50].

Let us consider the case when a soft wedge is left in the atmosphere of vapor pressure p_{ads} , so that an equilibrium adsorbed/wetting film of thickness H_{ads} is formed on its walls. The wedge walls are of constant thickness b_w . We assume that the wedge response is purely elastic and instant. It can be defined by its Young modulus E and Poisson ratio σ . The bending energy of the wedge can be written in the form [51]

$$\mathcal{E}[w^\dagger(x, y)] = \iint \left(D (\nabla^2 w^\dagger)^2 + T w^\dagger \right) dx dy, \quad (11)$$

where the first term is similar to Euler-Bernoulli elastica with w^\dagger being a deflection of the wall of the wedge, and a constant D being the flexural rigidity, $D = \frac{E b_w^3}{12(1 - \sigma^2)}$. The second term is a Lagrange multiplier accounting for a capillary pressure-induced traction $T = \gamma \nabla^2 h$ applied to the

wall of the wedge. Minimization of (11) leads to the biharmonic Kirchhoff-Love equation defining the steady-state of the wedge [51]:

$$D\nabla^2\nabla^2w^\dagger - T = 0. \quad (12)$$

Since the wedge in the following consideration is not connected to any liquid pool, the liquid profile along the wedge is translationally invariant: $w^\dagger = w^\dagger(\bar{x})$. Therefore, equation (12) is reduced to

$$D\frac{d^4w^\dagger}{d\bar{x}^4} - T = 0. \quad (13)$$

Equation (13), albeit with a different traction, has been recently used by Svetovoy et al. [52] to model an adhered cantilever bent by the van der Waals/Casimir forces. In our case of the soft wedge, the traction can be only obtained from the solution of the Derjaguin equation accounting for the possible deformation of the walls. The position of the liquid-gas interface is defined as $\bar{h} = \bar{H} + \bar{w} + \bar{w}^\dagger$ (Figure 11) and, therefore, equation reads

$$\frac{d^2\bar{H}}{d\bar{x}^2} = \bar{\Pi}(\bar{H}_{ads}) - \bar{\Pi}(\bar{H}) - \frac{d^2\bar{w}^\dagger}{d\bar{x}^2}, \quad (14)$$

Equation (14) is solved as a boundary value problem. In the case of the rigid wedge, the numerical solution can be controlled by comparing with analytical solution (7).

To write equation (13) in a dimensionless form, we use the scaling related to the range of the surface force action H_2 used in subsection 3.1. The deformation of the wedge wall and the wedge's wall thickness reads $\bar{w}^\dagger = \frac{w^\dagger}{H_2}$ and $\bar{b}_w = \frac{b_w}{H_2}$, accordingly. Defining the dimensionless elastocapillary length $\bar{\mathcal{L}}_c = \gamma \frac{1 - \nu^2}{EH_2}$, we can write the dimensionless traction exerted onto the wall by the liquid as $\bar{T} = \bar{\mathcal{L}}_c \frac{d^2\bar{h}}{d\bar{x}^2}$. Using equation (14), the traction \bar{T} can also be written as $\bar{T} = \bar{\mathcal{L}}_c [\bar{\Pi}(\bar{H}_{ads}) - \bar{\Pi}(\bar{H})]$. Thus, equation (13) can be rewritten using dimensionless variables as

$$\frac{d^4\bar{w}^\dagger}{d\bar{x}^4} - \mathcal{S} \frac{d^2\bar{h}}{d\bar{x}^2} = 0, \quad (15)$$

where $\mathcal{S} = \frac{12\bar{\mathcal{L}}_c}{\bar{b}_w^3} = \frac{12\gamma(1 - \nu^2)H_2^2}{Eb_w^3}$ is a softness parameter. The equation is solved as a boundary value problem. The boundary conditions at the symmetry axis are $\left. \frac{d\bar{w}^\dagger}{d\bar{x}} \right|_{\bar{x}=0} = 0$ and $\left. \frac{d^3\bar{w}^\dagger}{d\bar{x}^3} \right|_{\bar{x}=0} = 0$. The first boundary condition is due to the symmetry. The second boundary condition stands for the absence of a shear force at the symmetry axis. The right end of the wedge is considered to be simply supported and, therefore, we impose the following boundary conditions: $\bar{w}^\dagger(\bar{X}_w) = 0$ and $\left. \frac{d^2\bar{w}^\dagger}{d\bar{x}^2} \right|_{\bar{x}=\bar{X}_w} = 0$. The latter condition corresponds to the absence of the bending moment.

We note that in order to predict the large deformations, equation (15) has to be solved in iterations, so that the deformation corresponds to the traction induced by the liquid layer covering the deflected wall. Generally, 100 iterations were enough to reach a good convergence of the

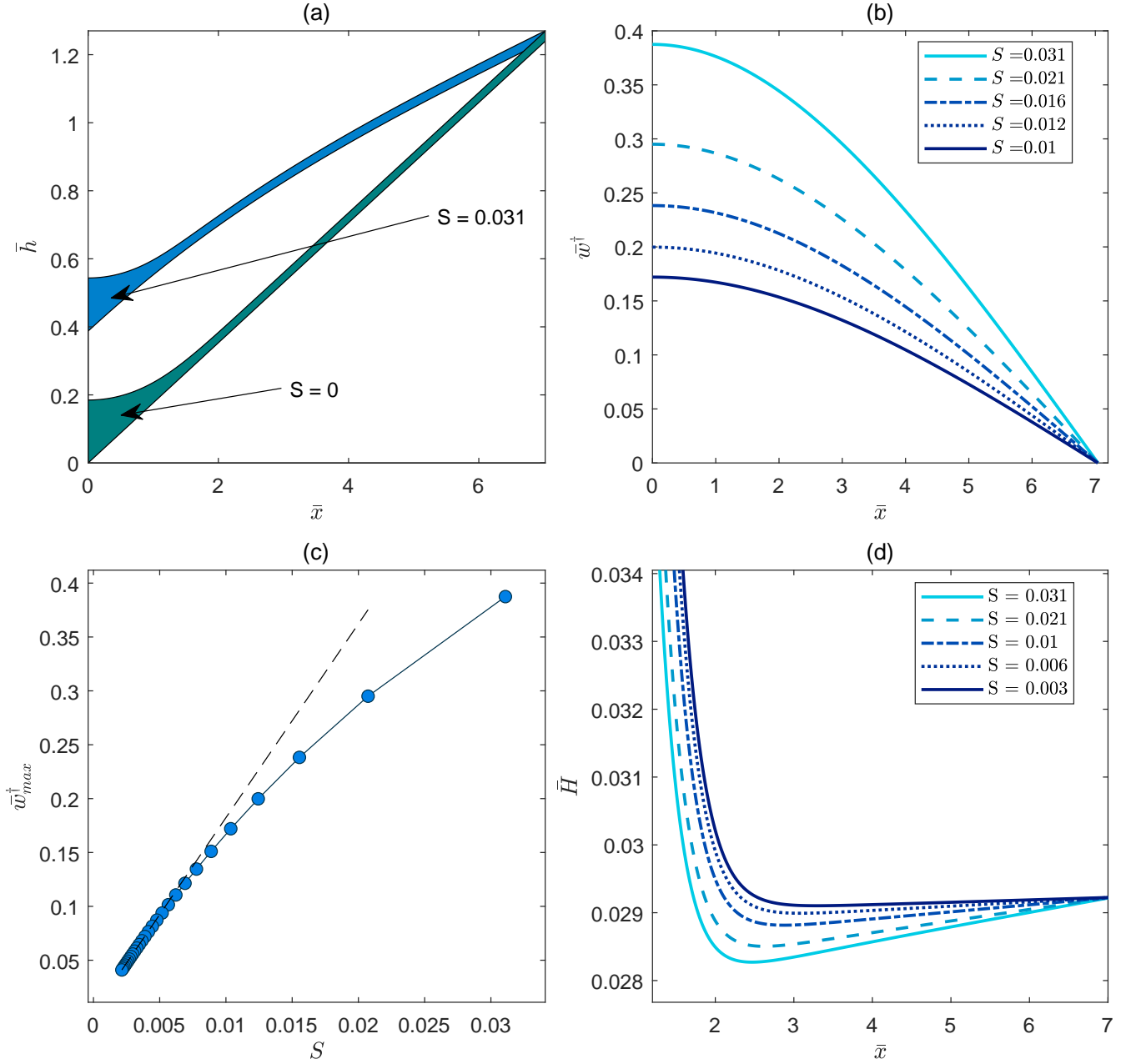


Figure 12: Wetting of the wedges with soft walls: (a) Rivulet profiles for soft ($\mathcal{S} = 0.031$) and rigid ($\mathcal{S} = 0$) walls; (b) Deflection of the wedge's wall for different values of softness parameter \mathcal{S} ; (c) Dependence of the maximal deformation \bar{w}_{max}^\dagger on the softness parameter \mathcal{S} ; (d) Thickness of the rivulet in the deformed wedges. The system behavior is defined by the isotherm A, $\beta = 2\theta_w$, $\phi = 0.7$.

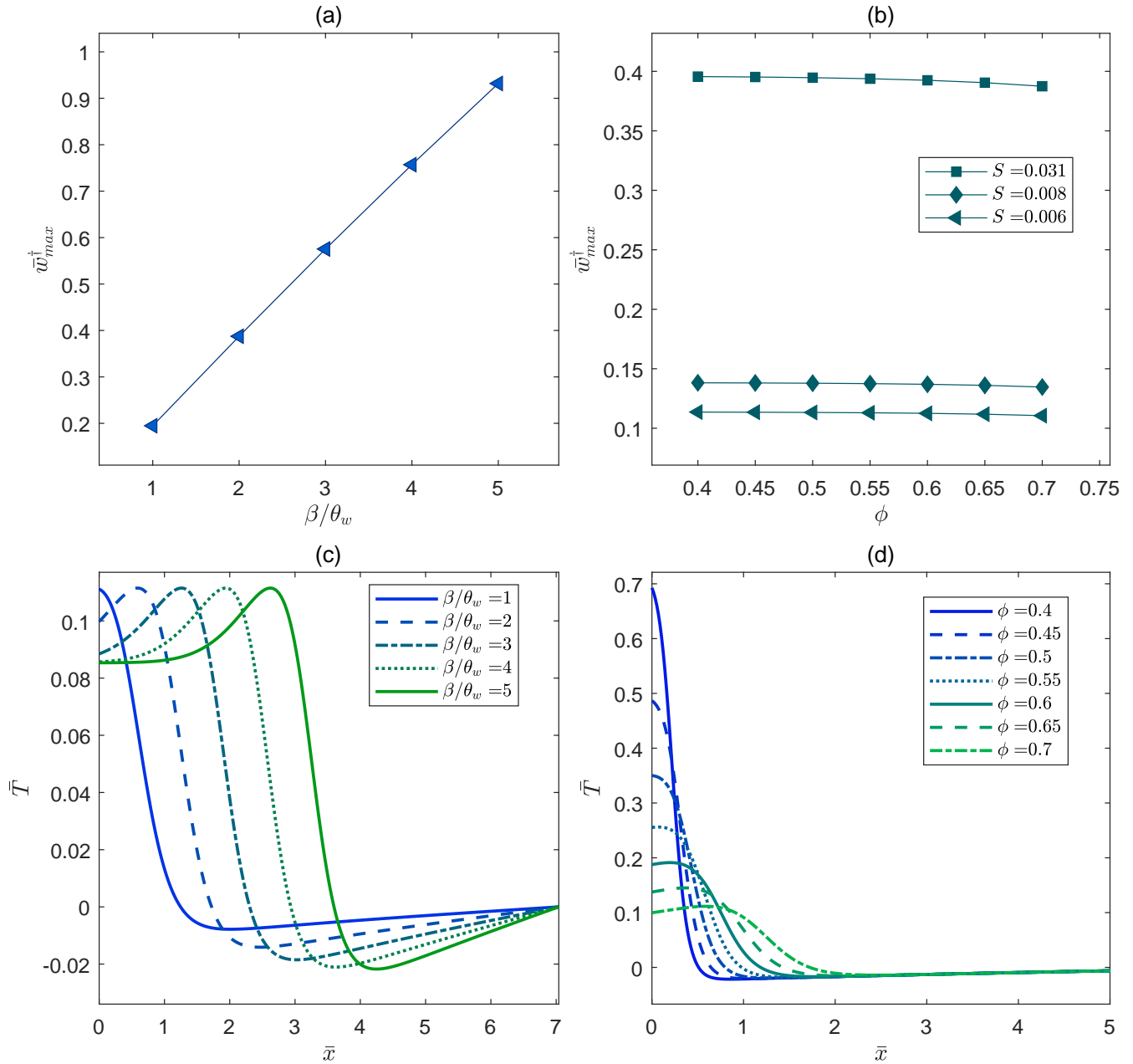


Figure 13: Wetting of the wedges with the soft walls. Dependence of the maximal deformation \bar{w}_{max}^\dagger on the (a) inclination angle ($S = 0.031$, $\phi = 0.7$), (b) on the wetting film thickness (parameter ϕ) ($S = 0.031$, $\beta = 2\theta_w$); (c) Traction exerted onto the walls of the wedge inclined by different β ($S = 0.031$, $\phi = 0.7$); (d) Traction exerted onto the walls of the wedge covered by the wetting film of different thickness ($S = 0.031$, $\beta = 2\theta_w$). The system behavior is defined by the isotherm A.

traction. The solutions of both equations (14) and (15) have been checked directly by numerical differentiation. The results have been in good agreement with those obtained by the numerical differentiation. The solver for obtaining the deflection has also been checked by comparison with the corresponding analytical solution of (15)

$$\bar{w}^\dagger = \frac{\mathcal{S}\bar{T}}{24} (5\bar{X}_w^4 - 6\bar{X}_w^2\bar{x}^2 + \bar{x}^4), \quad (16)$$

valid in the case when the traction \bar{T} is uniformly distributed over the wall of the wedge.

In Figure 12(a), the effect of the softness parameter on the shape of the rivulet is demonstrated. When the wedge walls are soft, the traction resulted from the interplay of the curvature-induced pressure and disjoining pressure deflects them and pull the wedge tip up. The deformation of the wedge's wall \bar{w}^\dagger is shown in Figure 12(b). As can be expected, the deformation becomes more pronounced for larger \mathcal{S} and is maximal at the symmetry axis, since the wedge ends are supported. The dependence of the maximal deformation of the wedge $\bar{w}_{max}^\dagger = \sup_{\bar{x} \in [0, \bar{X}_w]} \bar{w}^\dagger$ on the softness parameter \mathcal{S} is illustrated in Figure 12(c). It can be seen that the dependence is nearly linear for small \mathcal{S} (the linear trend is shown by a dashed black line). The changes of \bar{w}_{max}^\dagger depart from the linear trend for the softer wedges ($\mathcal{S} > 0.05$). Bending the wall of the wedge renders the region with $\bar{H} < \bar{H}_{ads}$ (Figure 12, d), on which the negative traction is exerted. The departure from the linear trend is, hence, related to the shape of the function $\mathcal{S}\bar{T}$.

The influence of the wedge inclination angle β and wetting film thickness \bar{H}_{ads} (corresponding parameter ϕ) on the maximal deformation and traction distribution \bar{T} is illustrated in Figure 13 (a-d). The increasing inclination angle β leads to the increasing deflection at the symmetry axis of the wedge. As can be seen in Figure 13(a), this dependence is linear. However, the effect of the inclination angle does not manifest itself via only the limiting thickness \bar{H}_w , as could be suggested. The limiting thickness \bar{H}_w increases with the increasing β . For $\beta/\theta_w > 2$, the limiting height is $\bar{H}_w \in (\bar{H}_{c1}; 1)$ (see schematic illustration in Supplementary Materials). Therefore, such increase of \bar{H}_w produces smaller traction at the symmetry axis (Figure 13, c). The maximal traction in those cases is $\bar{\Pi}(\bar{H}_{c1})$. The coordinate \bar{x} , where it is exerted onto the wall, is farther from the symmetry axis for the larger \bar{H}_w . That renders wider distributed (spread) traction and, hence, larger deformation, even though the the traction at the symmetry axis is smaller. For the case when $\beta/\theta_w = 1$, the limiting height \bar{H}_w lies very close to \bar{H}_{c1} , where the disjoining pressure isotherm finds its minimal value. Therefore, the maximal value of the traction is reached already at the symmetry axis which, in turn, renders a less spread traction.

The influence of the adsorbed/wetting film thickness (parameter ϕ) on the deformation \bar{w}_{max}^\dagger is presented in Figure 13(b). Since the formation of the film of thickness \bar{H}_{ads} is induced by the adsorption onto the walls of the wedge, we also plot a dependence of the maximal deformation of the wall of the wedge on the relative humidity RH of the atmosphere (Supplementary Materials). Unexpectedly, increasing humidity and, therefore, the adsorbed/wetting film thickness leads to the barely observable changes in the maximal deflection. The same trend was obtained for different values of \mathcal{S} . One can see from Figure 13(d) that for smaller \bar{H}_{ads} , the traction has a bigger amplitude \bar{T}_{max} , although it acts mainly in the vicinity of the symmetry axis. In turn, when \bar{H}_{ads} is larger, the traction has smaller \bar{T}_{max} albeit wider region of action. Thus, the negligibly small changes of \bar{w}_{max}^\dagger can result from the interplay of the traction amplitude and distribution.

The interplay of breadth of the region \bar{a} , over which the traction \bar{T} is distributed, and the

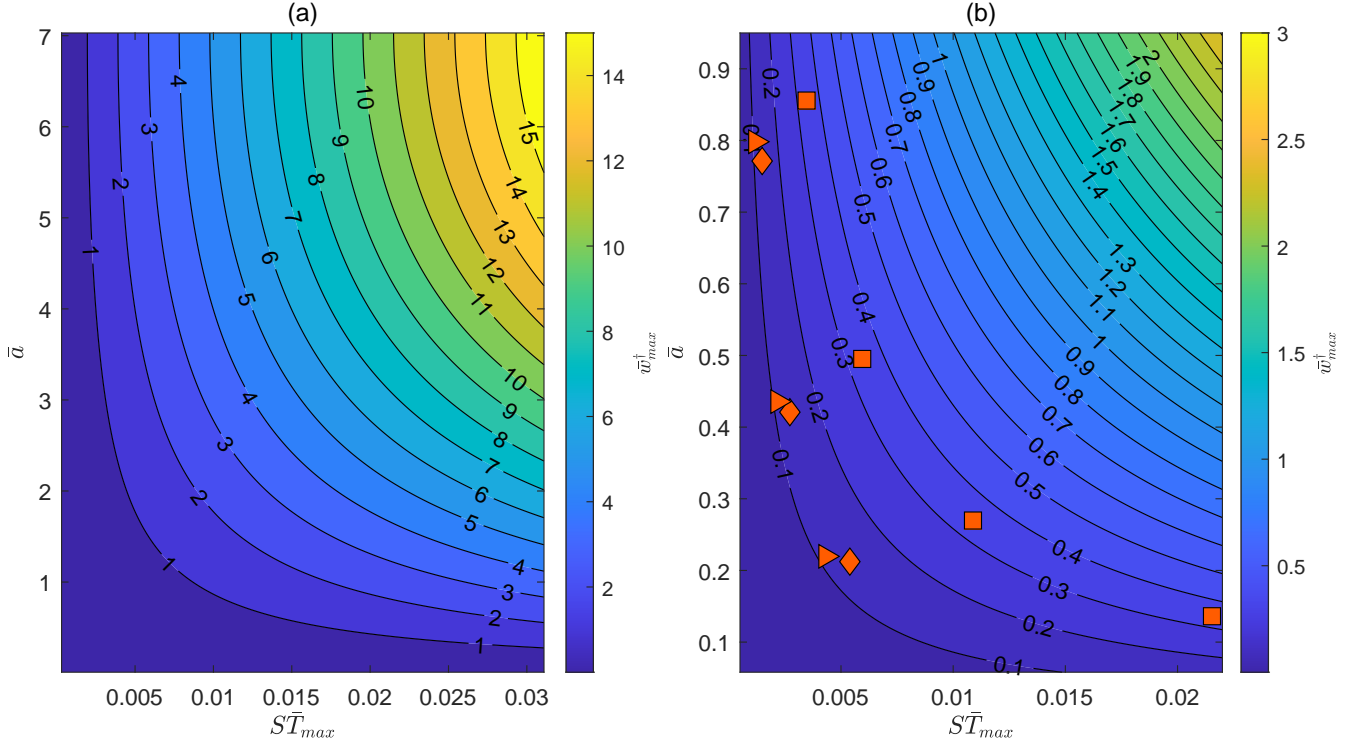


Figure 14: (a) The $\bar{\mathcal{S}}\bar{T}_{max}$ - \bar{a} -map of deformations obtained from solution (17); (b) Magnified region of the map for the small deformations. The analytical solutions for the cases with $\phi = 0.4, 0.5, 0.6, 0.7$ ($\mathcal{S} = 0.03$), $\phi = 0.4, 0.5, 0.6$ ($\mathcal{S} = 0.008$) and $\phi = 0.4, 0.5, 0.6$ ($\mathcal{S} = 0.006$) are shown by the orange squares, diamonds and triangles, accordingly. They can be compared to the numerically obtained deformations presented in Figure 13(b).

traction amplitude \bar{T}_{max} can be better understood from the simpler case suggested by Svetovoy et al. [52]. The traction can be modeled as a Heaviside function $\bar{T}_{max}\Theta(\bar{a} - \bar{x})$. Solving the corresponding equation $\frac{d^4\bar{w}^\dagger}{d\bar{x}^4} - \bar{\mathcal{S}}\bar{T}_{max}\Theta(\bar{a} - \bar{x}) = 0$, one can arrive at the deformation at the symmetry axis (see Supplementary Material for the solution):

$$\bar{w}_{max}^\dagger = \frac{\bar{\mathcal{S}}\bar{T}_{max}}{24} [5\bar{X}_w^4 + (\bar{a} - \bar{X}_w)^4 - 6\bar{X}_w^2(\bar{a} - \bar{X}_w)^2]. \quad (17)$$

The calculated deformations in the form of a $\bar{\mathcal{S}}\bar{T}_{max}$ - \bar{a} -map are shown in Figure 14(a, b). One can see that a concentrated traction with higher amplitude can still cause the same deformation as a spread traction having much smaller amplitude. In Figure 14(b), the analytical solutions for the cases with $\phi = 0.4, 0.5, 0.6, 0.7$ are shown by orange squares and triangles for $\mathcal{S} = 0.03$ and $\mathcal{S} = 0.006$, accordingly. The value of breadth \bar{a} cannot be obtained analytically. It has been evaluated using the numerical results as $\bar{a} = \frac{\int_0^{\bar{X}_w} \bar{T} d\bar{x}}{\sup_{\bar{x} \in [0, \bar{X}_w]} \bar{T}}$, so the forces per unit length exerted onto the wall of the wedge by the real traction (obtained numerically) and the Heaviside traction are equal. Although the deformations obtained analytically slightly depart from the numerical values (Figure 13, b), they generally support the findings, being located along the lines of the

equal deformations.

4 Conclusions

In the present work, we model edge wetting and discuss the shape of rivulets in rigid and soft open wedge channels. We show that when intermolecular interactions (surface forces) are taken into account, the validity of the well-known Concus-Finn condition breaks down. The steady-state rivulets can exist in the wedges even when the liquid-gas interface is concave. In order to obtain and quantify the rivulet profiles, we use the disjoining pressure concept and solve the Derjaguin equation. We demonstrate that the extent of the rivulet drastically depends on the humidity of the surrounding atmosphere, wedge geometry and surface force parameters.

We use Kirchhoff-Love theory in order to model the deformation of the soft wedge induced by the presence of the rivulet. We show that the relative humidity does not affect the deflection of the walls of the wedge, whereas the geometry of the wedge does.

We present simple analytical models allowing to predict the limiting height of the rivulet in the wedge and to estimate the deformation resulting from the interplay of the amplitude of the traction exerted onto the walls of the wedge and the breadth of the region, over which the traction is distributed.

Acknowledgements

The authors gratefully acknowledge the financial support from the Deutsche Forschungsgemeinschaft (DFG, German Research Foundation) – Priority Program “Dynamic Wetting of Flexible, Adaptive and Switchable Surfaces” (SPP 2171), Project Number 422792679.

Supplementary Materials

Disjoining pressure isotherm

The advantage of using the disjoining pressure isotherm containing a dispersive power-law part $\frac{A}{H^n}$ (n defines the dispersive repulsion/attraction) and a weak-overlap electrostatic/structural exponential tail $Ke^{-H/\chi}$ is the easier evaluation of H_1 , H_2 as well as its minima and maxima. The function $\Pi(H)$ is differentiable for $H \in (0; \infty)$ with the derivatives

$$\Pi^{(k)}(H) = (-1)^k \left(A \frac{\prod_{i=0}^{k-1} (n+i)}{H^{n+k}} - K \frac{e^{-H/\chi}}{\chi^k} \right), \quad (18)$$

where k is the order of the derivative. For the van der Waals forces, we have $n = 3$, whereas for the Casimir forces, we have $n = 4$. The roots of equation $\Pi^{(k)}(H) = 0$, that is

$$A \frac{\prod_{i=0}^{k-1} (n+i)}{H^{n+k}} - K \frac{e^{-H/\chi}}{\chi^k} = 0, \quad (19)$$

where $k \geq 1$, can be found using Lambert \mathcal{W} -function with branches $l = 0$ and $l = -1$, read as

$$H_{c\{k,l\}} = -(n+k)\chi\mathcal{W}_l \left[-\frac{1}{(n+k)\chi} \left(\frac{A\chi^k \prod_{i=0}^{k-1} (n+i)}{K} \right)^{\frac{1}{(n+k)}} \right] \quad (20)$$

For the case when $k = 0$, we obtain zeros of the disjoining pressure isotherm

$$H_{c\{0,0\}} = H_1 = -n\chi\mathcal{W}_0 \left[-\frac{1}{n\chi} \left(\frac{A}{K} \right)^{\frac{1}{n}} \right] \quad (21)$$

$$H_{c\{0,-1\}} = H_2 = -n\chi\mathcal{W}_{-1} \left[-\frac{1}{n\chi} \left(\frac{A}{K} \right)^{\frac{1}{n}} \right] \quad (22)$$

When $k = 1$, zeros of the derivative of the disjoining pressure isotherm read

$$H_{c\{1,0\}} = H_{c1} = -(n+1)\chi\mathcal{W}_0 \left[-\frac{1}{(n+1)\chi} \left(\frac{nA\chi}{K} \right)^{\frac{1}{(n+1)}} \right] \quad (23)$$

$$H_{c\{1,-1\}} = H_{c2} = -(n+1)\chi\mathcal{W}_{-1} \left[-\frac{1}{(n+1)\chi} \left(\frac{nA\chi}{K} \right)^{\frac{1}{(n+1)}} \right] \quad (24)$$

Inlet profile construction

The inlet profile is assumed to be macroscopic. Thus, it results from the solution of the Young-Laplace equation:

$$\frac{d^2\bar{h}(\bar{x})}{d\bar{x}^2} = \bar{p}_c, \quad (25)$$

where \bar{p}_c is the capillary pressure. The boundary conditions are $\frac{d\bar{h}}{d\bar{x}} = 0$ at $\bar{x} = 0$, $\bar{h} = \bar{H}_{ads} + \bar{X}_w \tan \beta$ at $\bar{x} = \bar{X}_w$. Integrating (25), one arrives at

$$\bar{h}(\bar{x}) = \bar{p}_c \frac{(\bar{x}^2 - \bar{X}_w^2)}{2} + \bar{X}_w \tan \beta + \bar{H}_{ads}. \quad (26)$$

This solution, however, does not satisfy the boundary condition for the Derjaguin equation for the rivulet, since it does not contain wetting film, to which the interface relaxes (Figure 15). Therefore, we must introduce a point x_t , where the transition to the wetting film occurs. Since the macroscopic profile does not immediately reaches the wetting film, at the transition point \bar{x}_t it has the thickness $\bar{H}_{ads} + c_1\bar{H}_{ads}$, where c_1 is a constant. Equation (26) will be rewritten as

$$\bar{h}(\bar{x}) = \bar{p}_c \frac{(\bar{x}^2 - \bar{x}_t^2)}{2} + \bar{x}_t \tan \beta + \bar{H}_{ads} + c_1\bar{H}_{ads}. \quad (27)$$

The value of the capillary pressure can be found from the condition on the contact angle θ_w : $\frac{d\bar{h}}{d\bar{x}} = \tan(\beta - \theta_w)$ at $\bar{x} = \bar{x}_t$. The capillary pressure is obtained as $\bar{p}_c = \frac{\tan(\beta - \theta_w)}{\bar{x}_t}$, and the shape of the interface for $\bar{x} \leq \bar{x}_t$ is written

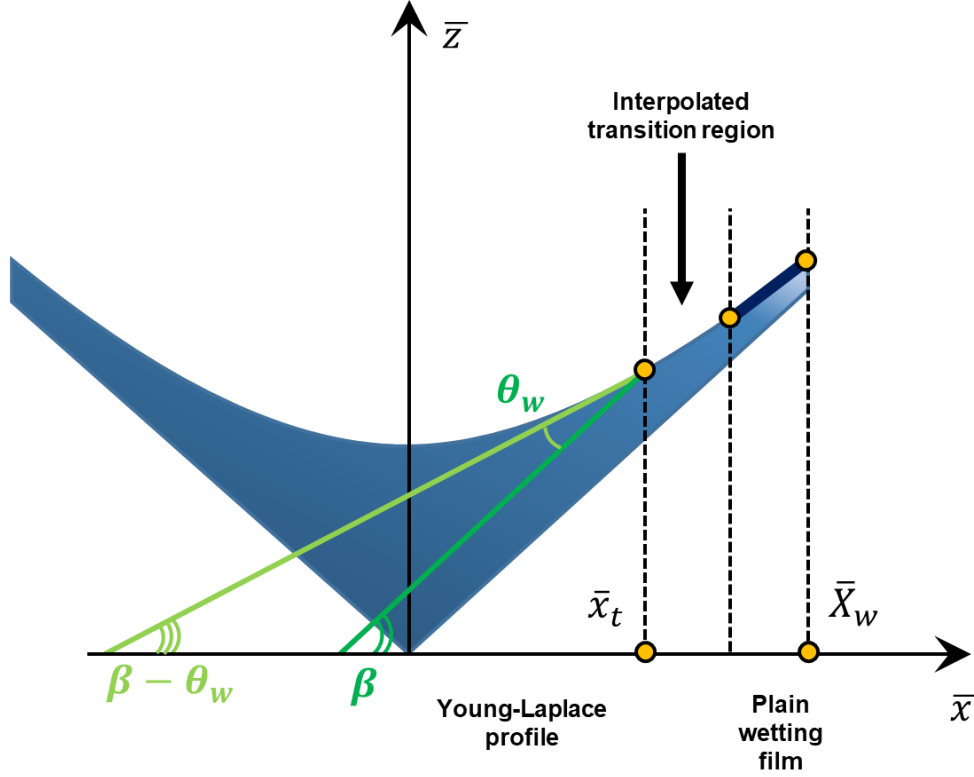


Figure 15: Schematic representation of the inlet profile.

$$\bar{h}(\bar{x}) = \frac{\tan(\beta - \theta_w)}{\bar{x}_t} \frac{(\bar{x}^2 - \bar{x}_t^2)}{2} + \bar{x}_t \tan \beta + \bar{H}_{ads} + c_1 \bar{H}_{ads}. \quad (28)$$

In order to make the transition smooth, we assume that the interface is the plane wetting film when $\bar{x} \geq \bar{x}_t + c_2 (\bar{X}_w - \bar{x}_t)$ and interpolate the region $\bar{x} \in (\bar{x}_t; \bar{x}_t + c_2 (\bar{X}_w - \bar{x}_t))$.

The parameters \bar{x}_t , c_1 , and c_2 of the inlet profile 28 used for the simulations are presented in Table 2. Slight variation of the parameters did not lead to significant changes in $\bar{H}(0, \bar{y})$.

Limiting height of the rivulet for the linearized disjoining pressure isotherm

When the wetting film is very thin: $\bar{H}_{ads} = \phi \bar{H}_1$ with $\phi \ll 1$, one can expect the limiting height of the rivulet \bar{H}_w to be smaller than the height \bar{H}_{c1} (from 23 with $n = 3$)

$$H_{c1} = -4\chi\mathcal{W}_0 \left[-\frac{1}{4\chi^{\frac{3}{4}}} \left(\frac{3A}{K} \right)^{\frac{1}{4}} \right], \quad (29)$$

where the disjoining pressure isotherm finds its minimum.

In this case, consideration of only the first stable branch of the disjoining pressure isotherm is sufficient. Due to its shape, this branch can be fairly represented by a straight line connecting points $(\bar{H}_{ads}; \Pi(\bar{H}_{ads}))$ and $(\bar{H}_w; \Pi(\bar{H}_w))$ where $\Pi(\bar{H}_w)$ (Figure 16, a). We also assume that

\bar{x}_t	c_1	c_2	Geometry
Data in Figures 3-5, 7, 10			
$0.95\bar{X}_w$	0.6	0.650	All configurations presented
Data in Figure 8			
$0.950\bar{X}_w$	0.6	0.650	$\bar{X}_w = 7.0, \beta = \theta, \phi = 0.3$
$0.631\bar{X}_w$	0.3	0.030	$\bar{X}_w = 7.0, \beta = 2\theta, \phi = 0.3$
$0.465\bar{X}_w$	0.3	0.030	$\bar{X}_w = 7.0, \beta = 3\theta, \phi = 0.3$
$0.364\bar{X}_w$	0.3	0.025	$\bar{X}_w = 7.0, \beta = 4\theta, \phi = 0.3$
$0.294\bar{X}_w$	0.3	0.015	$\bar{X}_w = 7.0, \beta = 5\theta, \phi = 0.3$
Data in Figure 9			
$0.950\bar{X}_w$	0.6	0.650	$\bar{X}_w = 7.0, \beta = 2\theta, \phi = 0.5$
$0.950\bar{X}_w$	0.6	0.600	$\bar{X}_w = 10.6, \beta = 2\theta, \phi = 0.5$
$0.950\bar{X}_w$	0.6	0.550	$\bar{X}_w = 14.1, \beta = 2\theta, \phi = 0.5$
$0.950\bar{X}_w$	0.6	0.500	$\bar{X}_w = 17.6, \beta = 2\theta, \phi = 0.5$
$0.950\bar{X}_w$	0.6	0.450	$\bar{X}_w = 21.1, \beta = 2\theta, \phi = 0.5$
$0.950\bar{X}_w$	0.6	0.380	$\bar{X}_w = 24.6, \beta = 2\theta, \phi = 0.5$
$0.950\bar{X}_w$	0.6	0.350	$\bar{X}_w = 28.2, \beta = 2\theta, \phi = 0.5$

Table 2: Parameters of the inlet profile 28 used for the simulations.

simplified isotherm crosses \bar{H} -axis in the immediate vicinity to \bar{H}_1 so it can be assumed that the point $(\bar{H}_1, 0)$ belongs to this straight line.

Equation

$$\frac{\tan^2 \beta}{2} = \bar{\Pi}(\bar{H}_{ads}) (\bar{H}_w - \bar{H}_{ads}) - \int_{\bar{H}_{ads}}^{\bar{H}_w} \bar{\Pi}(\bar{H}) d\bar{H} \quad (30)$$

can be rewritten in the following form

$$\tan^2 \beta = 2\bar{\Pi}(\bar{H}_{ads}) (\bar{H}_w - \bar{H}_1) + 2\bar{\Pi}(\bar{H}_{ads}) (\bar{H}_1 - \bar{H}_{ads}) - 2 \int_{\bar{H}_{ads}}^{\bar{H}_w} \bar{\Pi}(\bar{H}) d\bar{H}, \quad (31)$$

where the last term can be easily evaluated when the disjoining pressure isotherm is linearized (Figure 16, b)

$$2 \int_{\bar{H}_{ads}}^{\bar{H}_w} \bar{\Pi}(\bar{H}) d\bar{H} = \bar{\Pi}(\bar{H}_{ads}) \left[(\bar{H}_1 - \bar{H}_{ads}) - \frac{(\bar{H}_w - \bar{H}_1)^2}{\bar{H}_1 - \bar{H}_{ads}} \right]. \quad (32)$$

After some elementary arithmetical operations with (31) and (32), one obtains

$$(\bar{H}_w - \bar{H}_{ads})^2 = \frac{\tan^2 \beta (\bar{H}_1 - \bar{H}_{ads})}{\bar{\Pi}(\bar{H}_{ads})}, \quad (33)$$

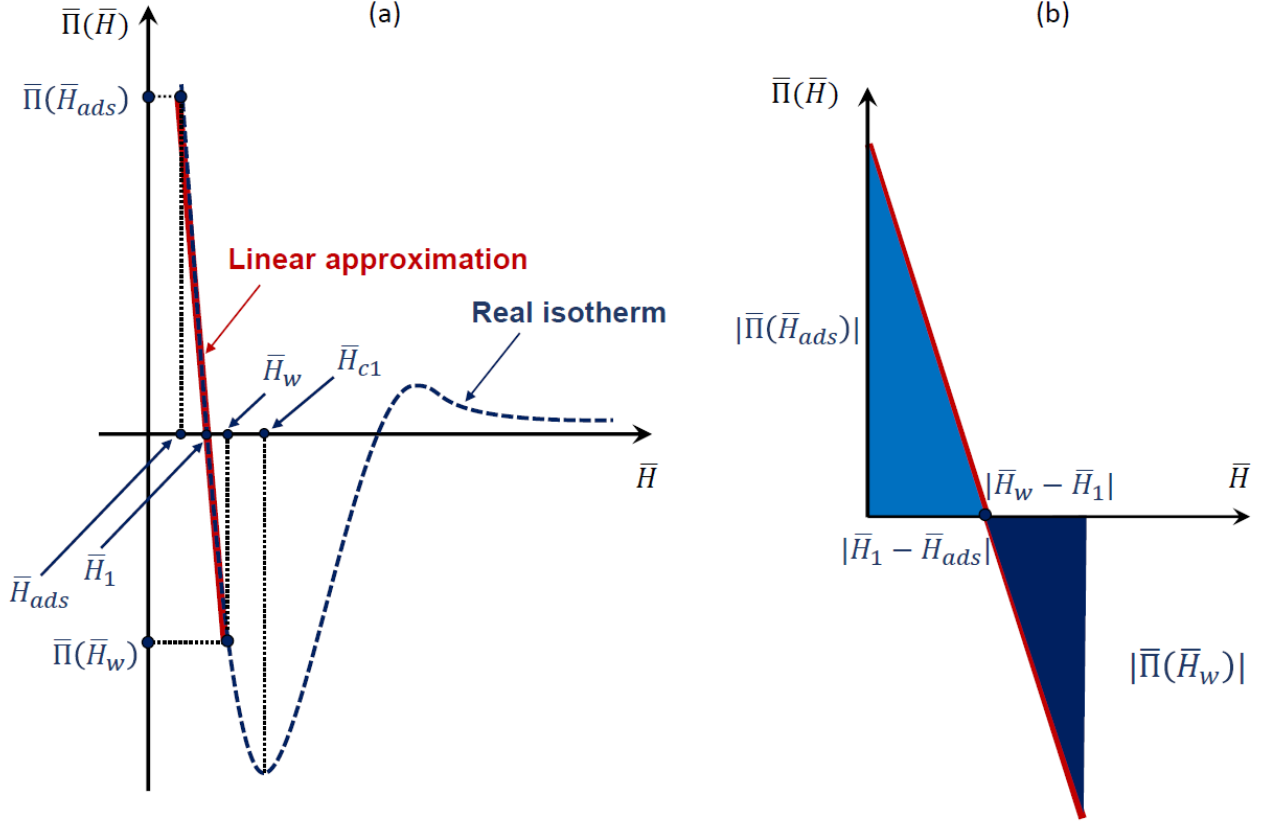


Figure 16: (a) Schematic representation of the disjoining pressure isotherm (dashed dark blue line) and its linearized branch (thick solid red line); (b) region used for the evaluation of integral in (30).

or, introducing the parameter ϕ ,

$$\bar{H}_w = \phi \bar{H}_1 + \tan \beta \sqrt{\frac{\bar{H}_1(1-\phi)}{\bar{\Pi}(\phi \bar{H}_1)}} = \bar{H}_{ads} + \tan \beta \sqrt{\zeta^{-2}}, \quad (34)$$

where $-\zeta^2$ is the slope of the first branch of the simplified disjoining pressure isotherm. Thus, among two rivulets having the same wetting film thickness \bar{H}_{ads} , the limiting height \bar{H}_w can be expected to be smaller for the rivulet, whose disjoining pressure isotherm has a larger slope of the first stable branch (alpha-branch).

The limiting height \bar{H}_w evaluated using equation (34) is presented in Figure 17 alongside the numerical results. The dashed black line depicts \bar{H}_{c1} setting the limiting ϕ , at which the assumptions used for (34) are valid. It can be seen that (34) generally predicts the dependence well for $\phi \gtrsim 0.5$, even despite the fact that the actual shape of the disjoining pressure isotherm has been ignored. We highlight that for the sake of simplicity, we have not accounted for the height dependence of the surface tension, although films with $\phi < 0.25$ are thinner than 1 nm.

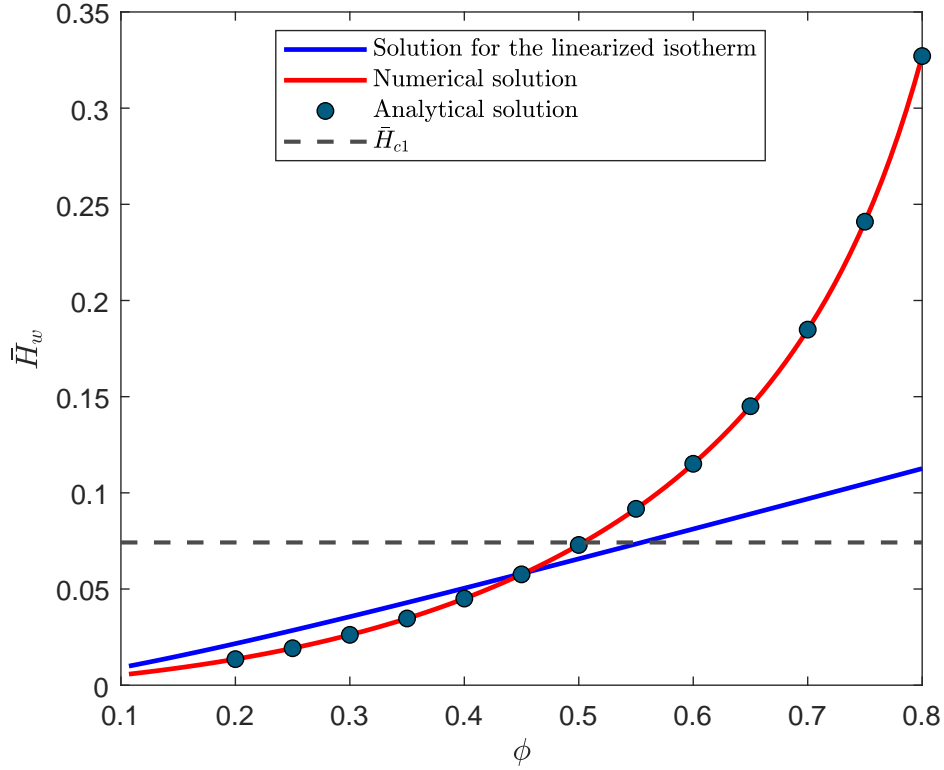


Figure 17: Dependence of the limiting height \bar{H}_w of the rivulet on ϕ . Blue solid line corresponds to the solution of equation (34), teal circle markers correspond to \bar{H}_w obtained from the analytical solution of the Derjaguin equation (as described in the manuscript, Eq. (7) and Eq. (8)), solid red line corresponds to H_w obtained from the numerical solution of the Derjaguin equation (solved as a boundary value problem). The isotherm A has been employed for the calculations.

Deformation of the soft wedge:

Solution of Kirchhoff-Love equation for a Heaviside traction

Let us consider the case when a step-like traction exerted onto the substrate near its end, in the region $\bar{x} \in [0; \bar{a}]$. The traction can be modeled as a Heaviside function $\bar{T} = \bar{T}_{max} \Theta(\bar{a} - \bar{x})$ of amplitude \bar{T}_{max} . The solid will respond to the traction by deflecting. The deflection \bar{w}^\dagger satisfies the Kirchhoff-Love equation:

$$\frac{d^4 \bar{w}^\dagger}{d\bar{x}^4} - \mathcal{S} \bar{T}_{max} \Theta(\bar{a} - \bar{x}) = 0. \quad (35)$$

We rewrite 35 using Laplace transforms. For the fourth derivative, we have

$$\mathcal{L} \left[\frac{d^4 \bar{w}^\dagger(\bar{x})}{d\bar{x}^4} \right] = s^4 \mathcal{L}[\bar{w}(\bar{x})] - s^3 \bar{w}^\dagger(0) - s^2 \bar{w}^{\dagger\prime}(0) - s \bar{w}^{\dagger\prime\prime}(0) - \bar{w}^{\dagger(3)}(0), \quad (36)$$

where primes denote the derivatives with respect to s . From the boundary conditions, we have $\bar{w}^{\dagger\prime}(0) = 0$ and $\bar{w}^{\dagger(3)}(0) = 0$. The Heaviside function can be written in the form

$$\Theta(\bar{a} - \bar{x}) = 1 - \Theta(\bar{x} - \bar{a}), \quad (37)$$

and its Laplace transform reads

$$\mathcal{L}[1 - \Theta(\bar{x} - \bar{a})] = \left(\frac{1}{s} - \frac{e^{-as}}{s} \right). \quad (38)$$

Therefore, we arrive at the equation in s -domain

$$\mathcal{L}[\bar{w}^\dagger(\bar{x})] = \frac{\mathcal{S}\bar{T}_{max} (1 - e^{-as})}{s^5} + \frac{w''(0)}{s^3} + \frac{w(0)}{s}, \quad (39)$$

which can be easily written in the original \bar{x} -domain by the reversed Laplace transform

$$\bar{w}^\dagger(\bar{x}) = \frac{1}{24}\mathcal{S}\bar{T}_{max} [\bar{x}^4 - (\bar{a} - \bar{x})^4\Theta(\bar{x} - \bar{a})] + \frac{\bar{x}^2}{2}\bar{w}^{\dagger''}(0) + \bar{w}^\dagger(0). \quad (40)$$

Due to the presence of the Heaviside function, it is more convenient to consider two intervals:

$$\bar{w}^\dagger(\bar{x}) = \begin{cases} \frac{1}{24}\mathcal{S}\bar{T}_{max} [\bar{x}^4 - (\bar{a} - \bar{x})^4] + \frac{\bar{x}^2}{2}\bar{w}^{\dagger''}(0) + \bar{w}^\dagger(0), & \text{if } \bar{x} \leq \bar{a} \\ \frac{1}{24}\mathcal{S}\bar{T}_{max}\bar{x}^4 + \frac{\bar{x}^2}{2}\bar{w}^{\dagger''}(0) + \bar{w}^\dagger(0). & \text{if } \bar{x} > \bar{a}. \end{cases} \quad (41)$$

From the two boundary conditions left $\bar{w}^\dagger(\bar{X}_w) = 0$ and $\bar{w}^{\dagger''}(\bar{X}_w) = 0$, we obtain

$$\bar{w}^\dagger(0) = -\frac{\mathcal{S}\bar{T}_{max}\bar{X}_w^4}{24} + \frac{\mathcal{S}\bar{T}_{max}(\bar{a} - \bar{X}_w)^4}{24} - \frac{\mathcal{S}\bar{T}_{max}\bar{w}^{\dagger''}(0)\bar{X}_w^2}{2}, \quad (42)$$

$$\bar{w}^{\dagger''}(0) = \frac{\mathcal{S}\bar{T}_{max}(\bar{a} - \bar{X}_w)^2}{2} - \frac{\mathcal{S}\bar{T}_{max}\bar{X}_w^2}{2}. \quad (43)$$

The deformation at the symmetry axis reads

$$\bar{w}^\dagger(0) = \frac{\mathcal{S}\bar{T}_{max}}{24} [5\bar{X}_w^4 + (\bar{a} - \bar{X}_w)^4 - 6\bar{X}_w^2(\bar{a} - \bar{X}_w)^2]. \quad (44)$$

References

- [1] David Quéré. Wetting and roughness. *Annual Review of Materials Research*, 38(1):71–99, August 2008. doi: 10.1146/annurev.matsci.38.060407.132434. URL <https://doi.org/10.1146/annurev.matsci.38.060407.132434>.
- [2] Qian Yang, P. Z. Sun, L. Fumagalli, Y. V. Stebunov, S. J. Haigh, Z. W. Zhou, I. V. Grigorieva, F. C. Wang, and A. K. Geim. Capillary condensation under atomic-scale confinement. *Nature*, 588(7837):250–253, December 2020. doi: 10.1038/s41586-020-2978-1. URL <https://doi.org/10.1038/s41586-020-2978-1>.

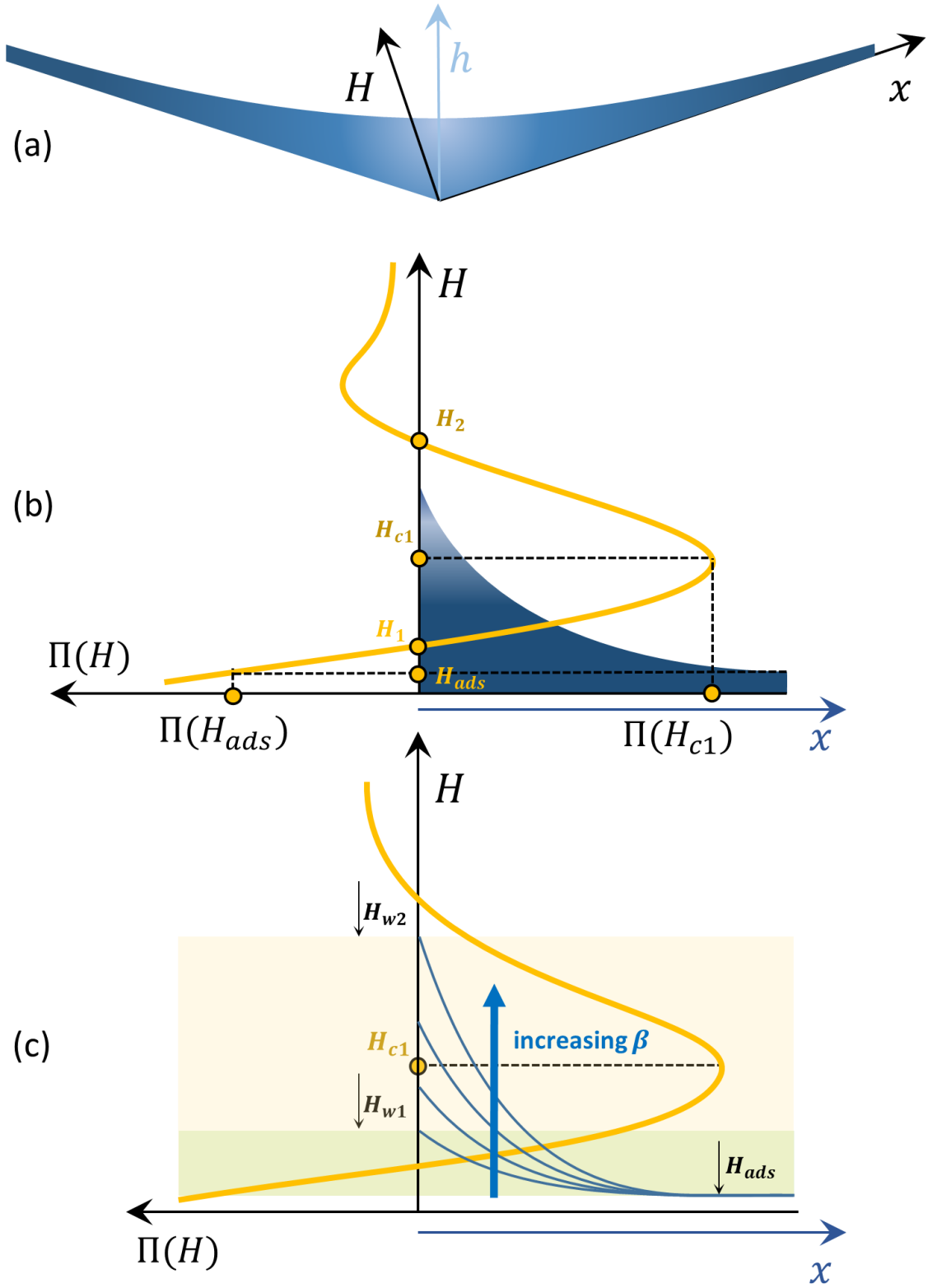


Figure 18: (Schematic representation (a) of the wedge; (b) of the distribution of the disjoining pressure over the wedge; (c) influence of the increasing wedge inclination angle on the distribution of the disjoining pressure over the wedge.

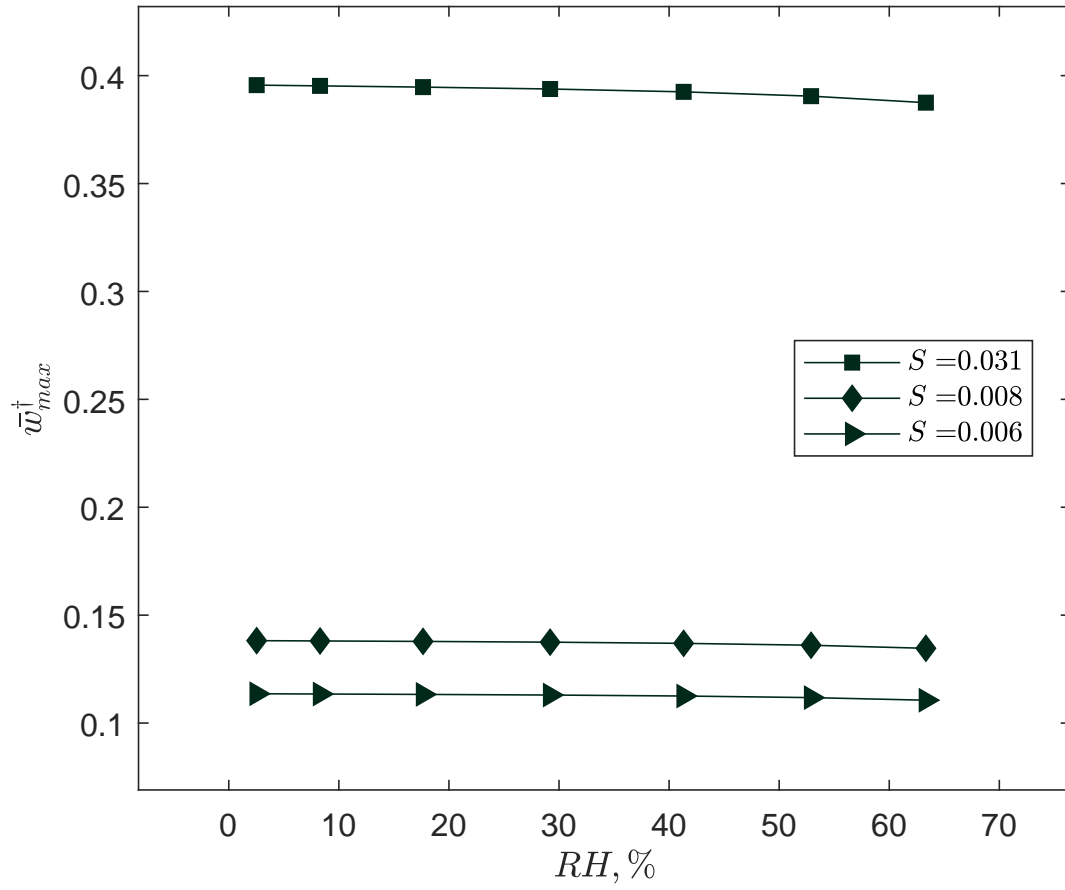


Figure 19: Influence of the relative humidity RH on the deformation of the wedge.

- [3] Jungchul Kim, Myoung-Woon Moon, Kwang-Ryeol Lee, L. Mahadevan, and Ho-Young Kim. Hydrodynamics of writing with ink. *Physical Review Letters*, 107(26), December 2011. doi: 10.1103/physrevlett.107.264501. URL <https://doi.org/10.1103/physrevlett.107.264501>.
- [4] Teresia Carreon, Elizabeth van der Merwe, Ronald L. Fellman, Murray Johnstone, and Sanjoy K. Bhattacharya. Aqueous outflow - a continuum from trabecular meshwork to episcleral veins. *Progress in Retinal and Eye Research*, 57:108–133, March 2017. doi: 10.1016/j.preteyeres.2016.12.004. URL <https://doi.org/10.1016/j.preteyeres.2016.12.004>.
- [5] Dahua Shou and Jintu Fan. Design of nanofibrous and microfibrinous channels for fast capillary flow. *Langmuir*, 34(4):1235–1241, January 2018. doi: 10.1021/acs.langmuir.7b01797. URL <https://doi.org/10.1021/acs.langmuir.7b01797>.
- [6] Minki Lee, Junho Oh, Hyuneui Lim, and Jinkee Lee. Enhanced liquid transport on a highly scalable, cost-effective, and flexible 3d topological liquid capillary diode. *Advanced Functional Materials*, page 2011288, March 2021. doi: 10.1002/adfm.202011288. URL <https://doi.org/10.1002/adfm.202011288>.
- [7] Kamaljit Singh, Michael Jung, Martin Brinkmann, and Ralf Seemann. Capillary-dominated fluid displacement in porous media. *Annual Review of Fluid Mechanics*, 51(1):429–449, January 2019. doi: 10.1146/annurev-fluid-010518-040342. URL <https://doi.org/10.1146/annurev-fluid-010518-040342>.
- [8] Tetsu K. Tokunaga. DLVO-based estimates of adsorbed water film thicknesses in geologic CO_2 reservoirs. *Langmuir*, 28(21):8001–8009, May 2012. doi: 10.1021/la2044587. URL <https://doi.org/10.1021/la2044587>.
- [9] Tatiana Gambaryan-Roisman. Liquids on porous layers: wetting, imbibition and transport processes. *Current Opinion in Colloid & Interface Science*, 19(4):320–335, August 2014. doi: 10.1016/j.cocis.2014.09.001. URL <https://doi.org/10.1016/j.cocis.2014.09.001>.
- [10] Markus Tuller, Dani Or, and Lynn M. Dudley. Adsorption and capillary condensation in porous media: Liquid retention and interfacial configurations in angular pores. *Water Resources Research*, 35(7):1949–1964, July 1999. doi: 10.1029/1999wr900098. URL <https://doi.org/10.1029/1999wr900098>.
- [11] Tian Yu, Jiajia Zhou, and Masao Doi. Capillary imbibition in a square tube. *Soft Matter*, 14(45):9263–9270, 2018. doi: 10.1039/c8sm01494a. URL <https://doi.org/10.1039/c8sm01494a>.
- [12] Vignesh Thammanna Gurumurthy, Daniel Rettenmaier, Ilia V. Roisman, Cameron Tropea, and Stephen Garoff. Computations of spontaneous rise of a rivulet in a corner of a vertical square capillary. *Colloids and Surfaces A: Physicochemical and Engineering Aspects*, 544:118–126, May 2018. doi: 10.1016/j.colsurfa.2018.02.003. URL <https://doi.org/10.1016/j.colsurfa.2018.02.003>.
- [13] M. M. Weislogel. Capillary flow in containers of polygonal section. *AIAA Journal*, 39(12):2320–2326, December 2001. doi: 10.2514/2.1237. URL <https://doi.org/10.2514/2.1237>.

- [14] Alexandre Ponomarenko, David Quéré, and Christophe Clanet. A universal law for capillary rise in corners. *Journal of Fluid Mechanics*, 666:146–154, January 2011. doi: 10.1017/s0022112010005276. URL <https://doi.org/10.1017/s0022112010005276>.
- [15] Tatiana Gambaryan-Roisman and Peter Stephan. Flow and stability of rivulets on heated surfaces with topography. *Journal of Heat Transfer*, 131(3), January 2009. doi: 10.1115/1.3056593. URL <https://doi.org/10.1115/1.3056593>.
- [16] Tatiana Gambaryan-Roisman. Simultaneous imbibition and evaporation of liquids on grooved substrates. *Interfacial Phenomena and Heat Transfer*, 7(3): 239–253, 2019. doi: 10.1615/interfacphenomheattransfer.2019031166. URL <https://doi.org/10.1615/interfacphenomheattransfer.2019031166>.
- [17] Francis Hauksbee. X. an account of an experiment touching the ascent of water between two glass planes, in an hyperbolick figure. *Philosophical Transactions of the Royal Society of London*, 27(336):539–540, December 1710. doi: 10.1098/rstl.1710.0071. URL <https://doi.org/10.1098/rstl.1710.0071>.
- [18] Paul Concus and Robert Finn. On the behavior of a capillary surface in a wedge. *Proceedings of the National Academy of Sciences*, 63(2):292–299, June 1969. doi: 10.1073/pnas.63.2.292. URL <https://doi.org/10.1073/pnas.63.2.292>.
- [19] Paul Concus and Robert Finn. Capillary surfaces in a wedge: Differing contact angles. *Microgravity Science and Technology*, 7(2):152–155, July 1994.
- [20] Paul Concus and Robert Finn. Discontinuous behavior of liquids between parallel and tilted plates. *Physics of Fluids*, 10(1):39–43, January 1998. doi: 10.1063/1.869547. URL <https://doi.org/10.1063/1.869547>.
- [21] Liquid bridges, edge blobs, and scherk-type capillary surfaces. 50(1):411–441, 2001. ISSN 00222518, 19435258. URL <http://www.jstor.org/stable/24901148>.
- [22] Kenneth A. Brakke. Minimal surfaces, corners, and wires. *Journal of Geometric Analysis*, 2(1):11–36, January 1992. doi: 10.1007/bf02921333. URL <https://doi.org/10.1007/bf02921333>.
- [23] Carlos Rascón, Andrew O. Parry, and Dirk G. A. L. Aarts. Geometry-induced capillary emptying. *Proceedings of the National Academy of Sciences*, 113(45):12633–12636, October 2016. doi: 10.1073/pnas.1606217113. URL <https://doi.org/10.1073/pnas.1606217113>.
- [24] Jean Berthier, Kenneth A. Brakke, and Erwin Berthier. A general condition for spontaneous capillary flow in uniform cross-section microchannels. 16:779–785, 01 2014. doi: 10.1007/s10404-013-1270-1. URL [10.1007/s10404-013-1270-1](https://doi.org/10.1007/s10404-013-1270-1).
- [25] J. Berthier, K.A. Brakke, E.P. Furlani, I.H. Karampelas, V. Poher, D. Gosselin, M. Cubizolles, and P. Pouteau. Whole blood spontaneous capillary flow in narrow v-groove microchannels. *Sensors and Actuators B: Chemical*, 206:258 – 267, 2015. ISSN 0925-4005. doi: <https://doi.org/10.1016/j.snb.2014.09.040>. URL <http://www.sciencedirect.com/science/article/pii/S0925400514011095>.

- [26] Francis Hauksbee. An account of an experiment touching the ascent of water between two glass planes, in an hyperbolick figure. *Philosophical Transactions (1683-1775)*, 27:539–540, 1710. ISSN 02607085. URL <http://www.jstor.org/stable/103171>.
- [27] Yu Tian, Ying Jiang, Jiajia Zhou, and Masao Doi. Dynamics of taylor rising. *Langmuir*, 35(15):5183–5190, March 2019. doi: 10.1021/acs.langmuir.9b00335. URL <https://doi.org/10.1021/acs.langmuir.9b00335>.
- [28] José Bico and David Quéré. Rise of liquids and bubbles in angular capillary tubes. *Journal of Colloid and Interface Science*, 247(1):162–166, March 2002. doi: 10.1006/jcis.2001.8106. URL <https://doi.org/10.1006/jcis.2001.8106>.
- [29] Felix Gerlach, Jeanette Hussong, Ilia V Roisman, and Cameron Tropea. Capillary rivulet rise in real-world corners. *Colloids and Surfaces A: Physicochemical and Engineering Aspects*, 592:124530, May 2020. doi: 10.1016/j.colsurfa.2020.124530. URL <https://doi.org/10.1016/j.colsurfa.2020.124530>.
- [30] M. Napiórkowski, W. Koch, and S. Dietrich. Wedge wetting by van der waals fluids. *Physical Review A*, 45(8):5760–5770, April 1992. doi: 10.1103/physreva.45.5760. URL <https://doi.org/10.1103/physreva.45.5760>.
- [31] K. Rejmer, S. Dietrich, and M. Napiórkowski. Filling transition for a wedge. *Physical Review E*, 60(4):4027–4042, October 1999. doi: 10.1103/physreve.60.4027. URL <https://doi.org/10.1103/physreve.60.4027>.
- [32] C. Rascón, J. Pausch, and A. O. Parry. First-order wedge wetting revisited. *Soft Matter*, 14(15):2835–2845, 2018. doi: 10.1039/c8sm00342d. URL <https://doi.org/10.1039/c8sm00342d>.
- [33] Maximilian Mußotter and Markus Bier. Wedge wetting by electrolyte solutions. *Physical Review E*, 96(3), September 2017. doi: 10.1103/physreve.96.032605. URL <https://doi.org/10.1103/physreve.96.032605>.
- [34] Harris Wong, S Morris, and C.J Radke. Three-dimensional menisci in polygonal capillaries. *Journal of Colloid and Interface Science*, 148(2):317–336, February 1992. doi: 10.1016/0021-9797(92)90171-h. URL [https://doi.org/10.1016/0021-9797\(92\)90171-h](https://doi.org/10.1016/0021-9797(92)90171-h).
- [35] B. V. Derjaguin, N. V. Churaev, and V. M. Muller. *Surface Forces*. Springer US, 1987. doi: 10.1007/978-1-4757-6639-4. URL <https://doi.org/10.1007/978-1-4757-6639-4>.
- [36] Victor M. Starov, Manuel G. Velarde, and Clayton J. Radke. *Wetting and Spreading Dynamics*. CRC Press, April 2007. doi: 10.1201/9781420016178. URL <https://doi.org/10.1201/9781420016178>.
- [37] Haoli Guo, Negar Nazari, Soheil Esmailzadeh, and Anthony R. Kocsiek. A critical review of the role of thin liquid films for modified salinity brine recovery processes. *Current Opinion in Colloid & Interface Science*, 50:101393, December 2020. doi: 10.1016/j.cocis.2020.101393. URL <https://doi.org/10.1016/j.cocis.2020.101393>.

- [38] Linyang Zhang, Xinran Yu, Zhangxin Chen, Jing Li, Gang Hui, Min Yang, and Rui Yu. Capillary dynamics of confined water in nanopores: The impact of precursor films. *Chemical Engineering Journal*, 409:128113, April 2021. doi: 10.1016/j.cej.2020.128113. URL <https://doi.org/10.1016/j.cej.2020.128113>.
- [39] A. O. Parry, C. Rascón, and A. J. Wood. Universality for 2d wedge wetting. *Physical Review Letters*, 83(26):5535–5538, December 1999. doi: 10.1103/physrevlett.83.5535. URL <https://doi.org/10.1103/physrevlett.83.5535>.
- [40] B. V. Deryagin, Ya. I. Rabinovich, and N. V. Churaev. Direct measurement of the structural component of the disjoining pressure. *Bulletin of the Academy of Sciences of the USSR Division of Chemical Science*, 31(8):1548–1553, August 1982. doi: 10.1007/bf00956890. URL <https://doi.org/10.1007/bf00956890>.
- [41] Martin Gielok, Marcus Lopes, Elmar Bonaccorso, and Tatiana Gambaryan-Roisman. Droplet on an elastic substrate: Finite element method coupled with lubrication approximation. *Colloids and Surfaces A: Physicochemical and Engineering Aspects*, 521:13–21, May 2017. doi: 10.1016/j.colsurfa.2016.08.001. URL <https://doi.org/10.1016/j.colsurfa.2016.08.001>.
- [42] V M Starov and M G Velarde. Surface forces and wetting phenomena. *Journal of Physics: Condensed Matter*, 21(46):464121, October 2009. doi: 10.1088/0953-8984/21/46/464121. URL <https://doi.org/10.1088/0953-8984/21/46/464121>.
- [43] Rafael Tadmor and Ken G. Pepper. Interfacial tension and spreading coefficient for thin films. *Langmuir*, 24(7):3185–3190, March 2008. doi: 10.1021/la702790b. URL <https://doi.org/10.1021/la702790b>.
- [44] Jacob N Israelachvili. *Intermolecular and surface forces; 3rd ed.* Academic Press, Amsterdam, 2011. URL <https://cds.cern.ch/record/1407176>.
- [45] N.V. Churaev and V.D. Sobolev. Prediction of contact angles on the basis of the frumkin-derjaguin approach. *Advances in Colloid and Interface Science*, 61:1–16, 1995. doi: 10.1016/0001-8686(95)00257-q. URL [https://doi.org/10.1016/0001-8686\(95\)00257-q](https://doi.org/10.1016/0001-8686(95)00257-q).
- [46] Calum J. Drummond and Derek Y. C. Chan. van der waals interaction, surface free energies, and contact angles: dispersive polymers and liquids. *Langmuir*, 13(14):3890–3895, July 1997. doi: 10.1021/la962131c. URL <https://doi.org/10.1021/la962131c>.
- [47] Jacob N. Israelachvili. The nature of van der waals forces. *Contemporary Physics*, 15(2):159–178, March 1974. doi: 10.1080/00107517408210785. URL <https://doi.org/10.1080/00107517408210785>.
- [48] Robert David and A. Wilhelm Neumann. A theory for the surface tensions and contact angles of hydrogen-bonding liquids. *Langmuir*, 30(39):11634–11639, September 2014. doi: 10.1021/la5027569. URL <https://doi.org/10.1021/la5027569>.

- [49] Toshihiko Tanaka, Mitsuaki Morigami, and Nobufumi Atoda. Mechanism of resist pattern collapse during development process. *Japanese Journal of Applied Physics*, 32(Part 1, No. 12B):6059–6064, dec 1993. doi: 10.1143/jjap.32.6059. URL <https://doi.org/10.1143/jjap.32.6059>.
- [50] Françoise Beltzung and Folker H. Wittmann. Role of disjoining pressure in cement based materials. *Cement and Concrete Research*, 35(12):2364–2370, December 2005. doi: 10.1016/j.cemconres.2005.04.004. URL <https://doi.org/10.1016/j.cemconres.2005.04.004>.
- [51] J. N. Reddy. *Energy Principles and Variational Methods in Applied Mechanics*. John Wiley I& Sons, 12 2017. ISBN 9781119087380.
- [52] V. B. Svetovoy, A. E. Melenev, M. V. Lokhanin, and G. Palasantzas. Global consequences of a local casimir force: Adhered cantilever. *Applied Physics Letters*, 111(1):011603, July 2017. doi: 10.1063/1.4991968. URL <https://doi.org/10.1063/1.4991968>.